Fabrication Process Changes for Performance Improvement of a RF MEMS Resonator: Conformable Contact Lithography, Moiré Alignment, and Chlorine Dry Etching

by

Mark Sakai

B.S. Civil Engineering
United States Air Force Academy, 2003

SUBMITTED TO THE DEPARTMENT OF MATERIALS SCIENCE AND ENGINEERING
IN PARTIAL FULFILLMENT OF THE REQUIREMENTS FOR THE DEGREE OF

MASTER OF SCIENCE IN MATERIALS SCIENCE AND ENGINEERING
AT THE
MASSACHUSETTS INSTITUTE OF TECHNOLOGY

JUNE 2005

Signature of Author _____

Department of Materials Science and Engineering
May 18, 2005

Certified by _____

David J. Carter
Charles Stark Draper Laboratory
Thesis Supervisor

Certified by _____

Harry L. Tuller
Professor of Ceramics and Electronic Materials
Thesis Advisor

Accepted by _____

Gerbrand Ceder
R. P. Simmons Professor of Materials Science and Engineering
Chair, Departmental Committee on Graduate Students

[THIS PAGE INTENTIONALLY LEFT BLANK]

Fabrication Process Changes for Performance Improvement of a RF MEMS Resonator: Conformable Contact Lithography, Moiré Alignment, and Chlorine Dry Etching

by

Mark Sakai

Submitted to the Department of Materials Science and Engineering on May 18, 2005, in partial fulfillment of the requirements for the Degree of Master of Science in Materials Science and Engineering

Abstract

This thesis presents fabrication process improvements for a RF MEMS resonator for the purpose of improving the quality factor (Q) and extending the frequency range. The process changes include the use of conformable contact lithography (CCL) and chlorine-based dry etching for improved fine-feature patterning and moiré-based alignment techniques to allow for a non-self-aligned process. The resulting control over feature size and structure are expected to improve Q and enable higher frequency resonators.

A CCL process utilizing moiré alignment marks is described. An automated moiré-based alignment system using Labview software is presented which demonstrates sub-100 nm alignment accuracy for a single alignment mark. A full-wafer alignment experiment is described that demonstrates average pattern placement errors of $|0.187\ \mu m|$ and $|0.296 \mu m|$ for the x- and y-directions respectively. The experimental limitations are analyzed and suggested improvements to the system are detailed.

Chlorine dry etching experiments are conducted in order to produce a straight sidewall etch through the "stack" of resonator materials (chrome, aluminum nitride, and molybdenum). A combination of Cl_2/O_2, Cl_2/Ar, and CF_4/O_2 plasmas at low pressure (2 mTorr), high microwave/source power (500W), and a moderate DC bias (-150V) demonstrates a straight sidewall angle ($>80^o$ measured from horizontal) with no undercut for all layers of the stack.

RF resonators fabricated with these process modifications are presented. An average overlay error of 55 nm (110 nm min-max) is recorded for 11 devices located closest to the line between the alignment marks in an aligned release of the resonators. The design modifications enabled by the new process are described and the prospect for higher-frequency devices and higher-Q device performance is discussed.

Technical Supervisor: Dr. David J. Carter
Title: Senior Member of the Technical Staff

Thesis Advisor: Professor Harry L. Tuller
Title: Professor of Ceramics and Electronic Materials

[THIS PAGE INTENTIONALLY LEFT BLANK]

Acknowledgements

11 May 2005

To think that I could have even come close to completing this thesis on my own effort would be absurd. I would first like to thank the Lord Almighty for his many blessings including the opportunity given to me to study at MIT. I would also like to thank my parents, family, and friends for their encouragement and prayers. I am also indebted to my thesis supervisor, Dr. David Carter, and MEMS Group Leader, Dr. Amy Duwel, who helped me out of a tight spot by deciding to take a chance on someone who knew absolutely nothing about MEMS. I am especially grateful to David for his incredible patience and providing me with so much help even though he had far more important matters to attend to. I also would like to thank my thesis advisor, Prof. Harry Tuller, who was willing to take time out of his busy schedule to provide me with his time and input. I must also thank Joe Akin for helping me get in the door at Draper.

I would like to thank the members of the MEMS Group who helped me out along the way. Specifically, I would like to thank Connie Cardoso for the enormous amount of wafer processing she did for me. I also would like to thank Mirela Bancu and Dan Pulver for looking out for me in the fab. I also would like to thank the people in the Draper Education Office who made my stay at Draper possible: George Schmidt, Loretta Mitrano, and Joseph Sarcia. Thanks also to the Harvard University Center for Nanoscale Systems for the use of their cleanroom.

Additional thanks go to my AFIT supervisors and ROTC detachment 365 staff for helping me stay on top of my military obligations. Thanks also to DMSE administrator Kathleen Farrell who always seemed to have an answer for the multitude of questions that I had.

This thesis was prepared at The Charles Stark Draper Laboratory, Inc., under Internal Company Sponsored Research Project 12578-001, Nanoscale Fabrication and Applications.

Publication of this thesis does not constitute approval by Draper or the sponsoring agency of the findings or conclusions contained herein. It is published for the exchange and stimulation of ideas.

Mark Sakai

[THIS PAGE INTENTIONALLY LEFT BLANK]

Contents

Chapter 1
Introduction and Background

1.1 Introduction

The rapid growth of RF wireless applications has created spectrum crowding in the 500 MHz to 6 GHz frequency range and exposed the need for high-performance frequency-control devices. Applications in this frequency range include wireless communication, navigation, palmtop computers, GPS systems, and other types of data communication for commercial and military use [1]. In a wireless system, the key driver is to achieve a high signal-to-noise ratio on receive and emit as little interference as possible on transmit [2]. Thus, front-end filters that shield adjacent channel interference on receive and output filters that constrain bandwidth noise on transmit are of increasing need. Currently, RF transceivers rely on bulky, off-chip resonator technologies for frequency selectivity. The development of small, high quality factor (Q), IC-compatible resonators will greatly decrease the size and improve the performance of current wireless technologies. The MEMS Group at Draper Laboratory has developed a piezoelectric, longitudinal-bar (L-bar) MEMS resonator designed to operate in the ~0.5-3 GHz frequency range at high Q (~several thousand) [3]. This project has been ongoing for the past 3 years and thus far, devices with frequencies ranging from 150-900MHz with Q's as high as 1200 (for lower frequency devices) have been demonstrated [4,5]. The MEMS Group has recently developed a new mask design and fabrication process to improve the performance of the resonator. The objective of this thesis is to present fabrication process changes that were developed to improve the frequency range and Q factor of the resonators. These process changes are conformable contact lithography, moiré alignment, and chlorine dry etching.

1.2 Chapter Summary

This thesis is comprised of five chapters. In the remainder of Chapter 1, the background of the Draper L-bar resonator, performance barriers from the previous fabrication process, a new resonator design, and a new fabrication process are presented. In Chapter 2, conformable contact lithography (CCL), moiré alignment, and an automated alignment system are described. Theoretical and actual alignment accuracies are also reported. Chapter 3 discusses the implementation of a chlorine dry etch to the fabrication process and presents results of the new procedure. Chapter 4 presents device fabrication results of the new process. Finally, Chapter 5 summarizes the work that is presented, provides conclusions, and discusses suggestions for future work.

1.3 Background of Draper Piezoelectric MEMS Resonator

1.3.1 Resonator Design

The Draper L-bar resonator resembles a suspended capacitor in the shape of a rectangular bar. Figure 1.1 shows a schematic of the resonator suspended over a silicon substrate by tethers. The bar consists of a top metal electrode, a piezoelectric dielectric middle section, and a bottom metal electrode. Nickel was originally used as the top metal, but in later device fabrications, nickel vanadium (NiV) and chrome (Cr) were tested. Aluminum nitride (AlN) was selected as the piezoelectric and molybdenum (Mo) was used as the bottom metal. When a field is applied between the two electrodes through the thickness of the bar, the device stretches. The three fundamental longitudinal frequency stretching modes are the bar's length, width, and thickness. The length of the bar defines the resonant frequency [3]. Figure 1.2 demonstrates the designed mode of operation.

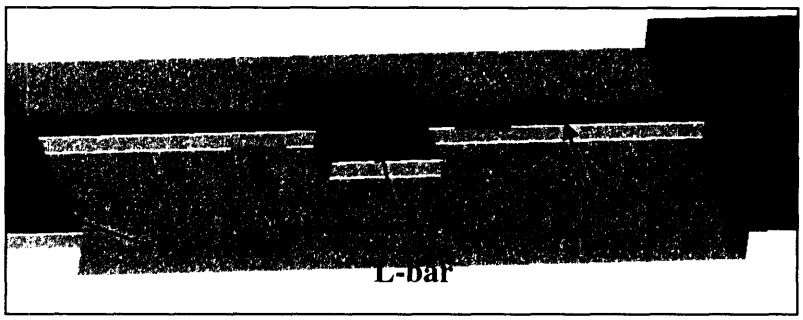

Figure 1.1: Schematic of suspended MEMS L-bar resonator.[1]

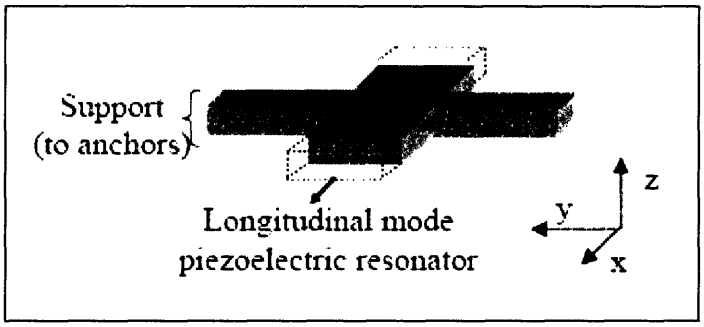

Figure 1.2: Resonator's intended mode of operation.[1]

When a field is applied across the electrodes at a frequency far from the mechanical resonance frequency the device has high impedance much like a capacitor. However, at the mechanical resonance frequency, the electrical impedance drops well below the normal capacitance impedance. This drop in impedance is directly related to the device's Q. The Butterworth Van-Dyke (BVD) model can be used as an equivalent circuit model to describe the resonator's impedance transfer function [6]. The BVD model looks similar to that of an RLC circuit in parallel with a capacitor as shown in Figure 1.3.

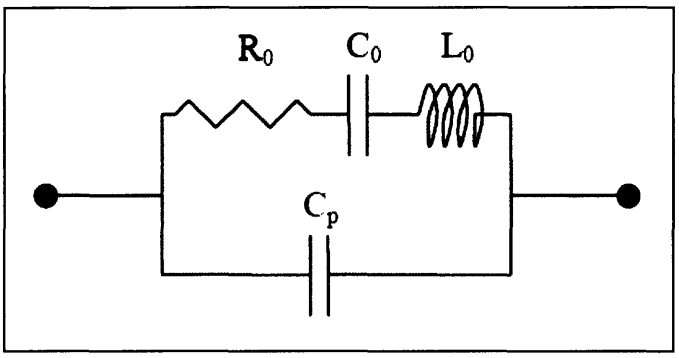

Figure 1.3: Butterworth Van-Dyke equivalent circuit model.[1]

The equivalent circuit parameters and resonant frequency are

$$R = \frac{t\pi}{Q}\frac{\sqrt{E\rho}}{8we^2} \qquad L = \frac{t\rho l}{8we^2} \qquad C = \frac{8we^2 l}{tE\pi^2} \qquad C_o = \frac{\varepsilon_z wl}{t} \qquad \frac{\omega_1}{2\pi} = \frac{1}{2L}\sqrt{\frac{E}{\rho}} \qquad (1.2.1)$$

where E = stiffness constant, ρ = density, e = piezoelectric coefficient, ε = dielectric constant, Q = quality factor, l = length of bar, w = width of bar, and t = thickness of bar. For the BVD model C_p represents the static capacitance. This is the capacitance of the electrodes and piezoelectric acting as one capacitor, ignoring motional effects. The R_o, C_o, and L_o branch of the model represents the mechanical vibrations of the circuit. At low frequencies the capacitors in each parallel circuit branch restrict current flow which results in high impedances. However, as frequency increases it eventually reaches the natural resonant frequency of the device. At this frequency, the effects of C_o and L_o in the mechanical vibration arm of the circuit cancel each other resulting in the minimum possible resistance of R_o.

Figure 1.4 demonstrates the longitudinal mode resonances for a bar with a length of 5.5 μm, width of 3 μm, and thickness of 0.5 μm, and Q of 1000 calculated using the BVD model. The bar width and thickness resonant frequencies are higher than that for the length and are spaced such that only one mode appears in the range of interest.

[1] Figure(s) courtesy of Dr. David J. Carter, MEMS Group, Draper Laboratory

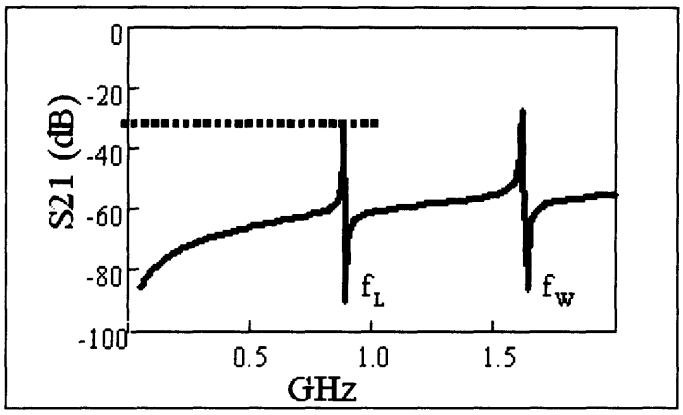

Figure 1.4: Well isolated length and width longitudinal mode resonances.[1]

The advantages of the Draper piezoelectric MEMS resonator allow for miniaturization and increased performance of wireless communication devices: First, the resonant frequency is defined by the in-plane dimensions of the resonator, which allows the fabrication of arrays of resonators with different frequencies to be fabricated on a single chip. This holds the potential for complex filter designs or fast frequency hopping. Second, the longitudinal length modes are resistant to thermal stress from packaging. Third, the device impedance can be scaled by changing the width of the resonator for impedance matching. Fourth, the resonator structure and use of AlN permits high Q designs. Aluminum nitride also holds several other key advantages such as a low deposition temperature, low dielectric loss tangent, high dielectric breakdown, and linear response. Finally, the device processing is IC compatible allowing for integration in transceiver applications [4].

1.3.2 Previous Fabrication Process

A schematic of the process flow used for devices reported in [4] is shown in Figure 1.5.

- The fabrication process begins with the following materials stack on a silicon wafer: a 0.5-1.0 μm thick thermally grown SiO_2 release layer, a ~200 Å "seed" layer of AlN, 1500 Å of Mo, and 5000 Å of polycrystalline, c-axis-oriented AlN. Next, ~1500 Å of top metal is patterned by evaporation and liftoff. Originally Ni

was used, but a magnetoelastic damping effect appeared to limit the Q of the device. Therefore, NiV and Cr were later selected as top metal alternatives.

- The next step in the process is to etch the mechanical structure by patterning through the materials stack. In this step, each layer in the stack serves as an etch mask for the layer below it: The top metal serves as the etch mask for the AZ400K wet etch of the AlN, the AlN is the etch mask for the CF_4/O_2 reactive ion etch (RIE) of the Mo, and the Mo is the mask for the wet etch of the AlN seed layer. The shape of the resonator, support tethers and probe pads are evident at this point.
- Next, the electrical circuit needs to be completed. An etch is made on one tether in the top metal and an undercut etch of the Mo is made on the other tether. This decreases parasitic capacitances by limiting the top and bottom metal overlap in areas around the resonator. The Ni and AlN on the probe pad opposite the undercut etch of the Mo are then wet etched to allow bottom metal access for testing. Finally, platinum patches applied by liftoff are placed to short the top and bottom metal islands on the tethers.
- Finally, the device is released by etching the SiO_2 in BHF.

The advantages of this fabrication process are the self-aligned nature of both the stack etch (each layer serves as an etch mask for the subsequent layers) and the release etch. An unintended consequence of this self-aligned release is an unsupported ledge around the bond pads, which may have an adverse impact on device Q. Additionally, the top and bottom metal cuts, required to minimize stray capacitance, add complexity to the process and reduce yield.

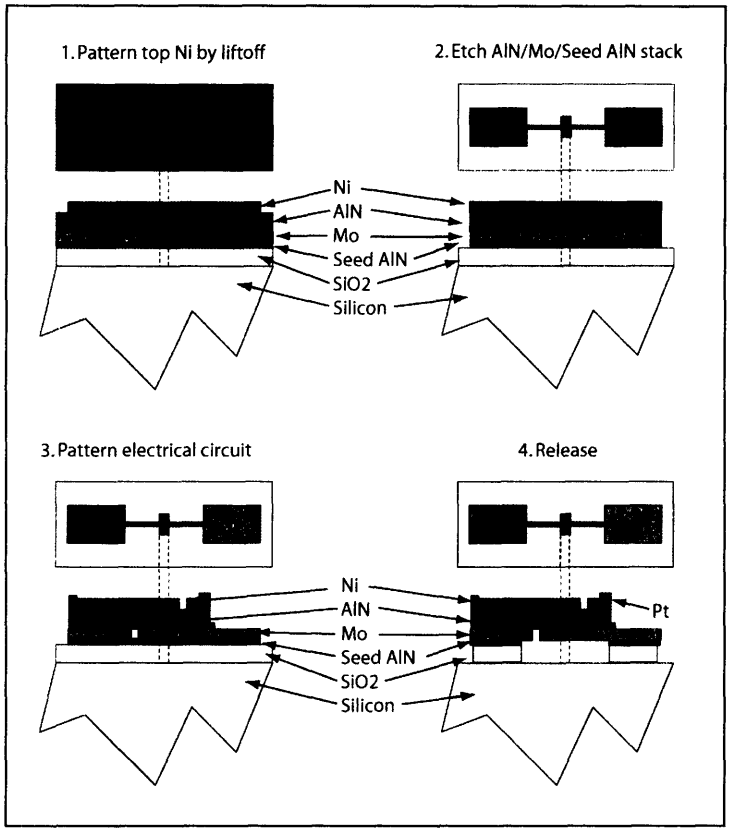

Figure 1.5: Fabrication process flow.[1]

1.3.3 Performance Goals

Previous modeling of the resonator design suggested that a high quality factor and low impedance in the GHz frequency range should be attainable. Thus far, measured quality factor and other electrical parameters have yet to achieve the levels that theoretical simulations would suggest. Recently measured resonator parameters are listed in Table 1.1.

Table 1.1: L-bar parameter measurements.[1]

Parameter	Current Data
Frequency range	150 MHz – 900 MHz
Precision of center frequency	5%
Quality factor	1200
Impedance at resonance	1750 Ω
Impedance ratio on/off resonance	15 dB

1.4 Performance Barriers

Ultimately, high-Q resonators in the GHz frequency range are desirable in order to meet current and future technology needs. The following subsections address process improvements to help meet these goals.

1.4.1 Q Improvement

Q is related to the energy losses from the resonator. Decreasing energy losses should increase Q. The resonator performance, in terms of its electrical impedance at resonance, depends critically on the resonator's mechanical connection to the substrate. It is believed that anchor damping (the energy that leaves the resonator through the tethers and device anchors at the substrate) is the main source of energy loss and Q limitations for the Draper L-bar resonator [5]. Possible contributors to anchor damping that are addressed by the fabrication changes are the elimination of a free-hanging ledge at the bond pads and minimization of energy losses at the resonator-tether interface.

In the original resonator design a free-hanging ledge at the bond pads was present due to the SiO_2 undercutting during the isotropic release etch. This ledge undergoes a "flapping" motion, which pollutes the resonance mode shape, propagates energy away from the system, and thus diminishes Q [7]. Figure 1.6 shows a simulation (performed in [7]) of the ledge profile and of the "flapping" motion.

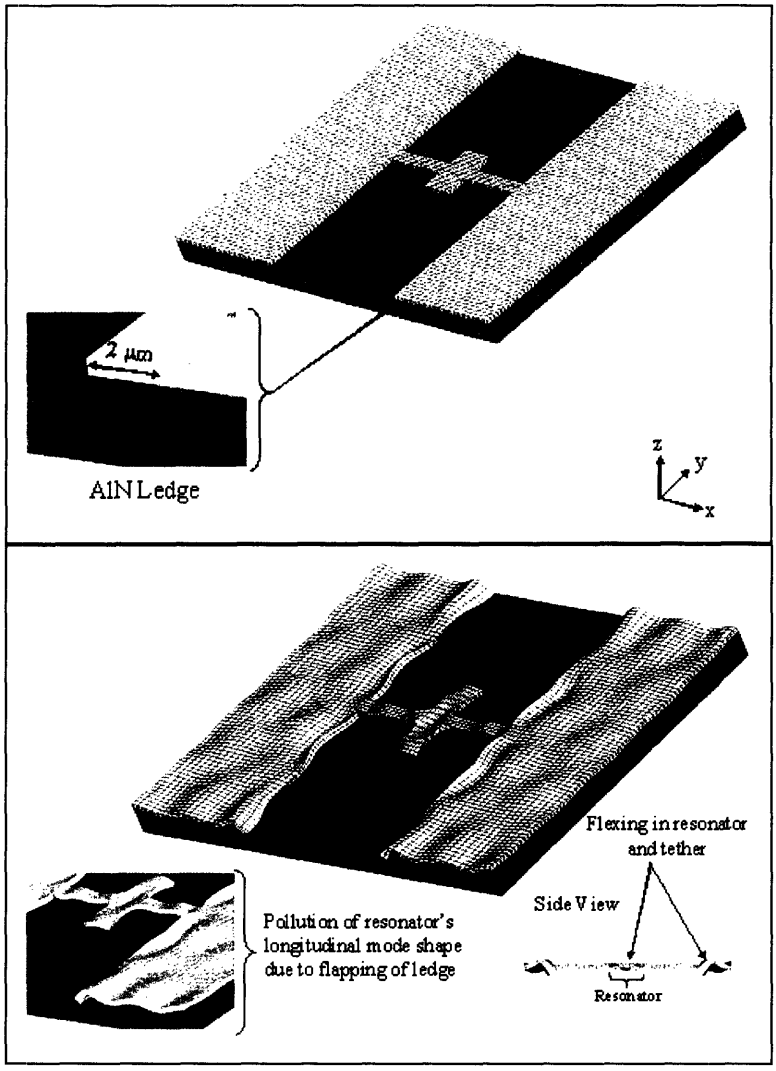

Figure 1.6: Top – Profile of the free hanging ledge produced by SiO_2 undercutting; **Bottom –** Simulated "flapping" motion of the ledge which pollutes the resonator's longitudinal mode shape [7].

By masking the release etch lithographically with an aligned opening in photoresist, the ledge can be eliminated and the tether will undergo a more abrupt mechanical transition

from free to rigidly attached to the underlying SiO_2. This should improve acoustical impedance mismatch and therefore reduce energy loss through the tethers.

In order to implement this process change, a precisely aligned release via CCL/moiré alignment is necessary. Alignment overlay accuracies of 100-200 nm have been demonstrated with conventional contact lithography in the Draper MEMS fab, but overlay accuracies on the order of 1-2 μm are more typical [5]. Simulations have shown that the optimum tether lengths for the L-bar resonator are odd multiples of a quarter wavelength, while the least optimal configuration is a tether length that is one-half a wavelength, λ [7]. The tether lengths should therefore be controlled to several times less than λ/4 (*i.e.* ~λ /10- λ/20). L-bar acoustic wavelengths in the 1-5 GHz range are λ=2-10 μm, so a reliable alignment scheme with overlay errors well below one micron is required for an aligned release for the L-bar.

Energy transmission to the tethers occurs at the resonator-tether interface. It is believed that this problem can be mitigated by the inclusion of notches at the interface (see Section 1.5). The notched attachments are small features and can only be produced with a straight sidewall etch (Cl-based dry etch) and a high resolution lithography method such as CCL. In the old fabrication process, the wet etch of the AlN produced sloped sidewalls (~60° measured from horizontal), which limits the size of the notches to ~0.57 μm.

1.4.2 Smaller Resonators/Higher Frequencies

Increasing the resonator frequency requires scaling down its in-plane dimensions as shown in Figure 1.7. The slope of the line is 3.7 GHz/μm which is consistent with the material properties of the resonator in longitudinal mode. Therefore, a resonator with a length of 1 μm is expected to have a resonant frequency near 4 GHz.

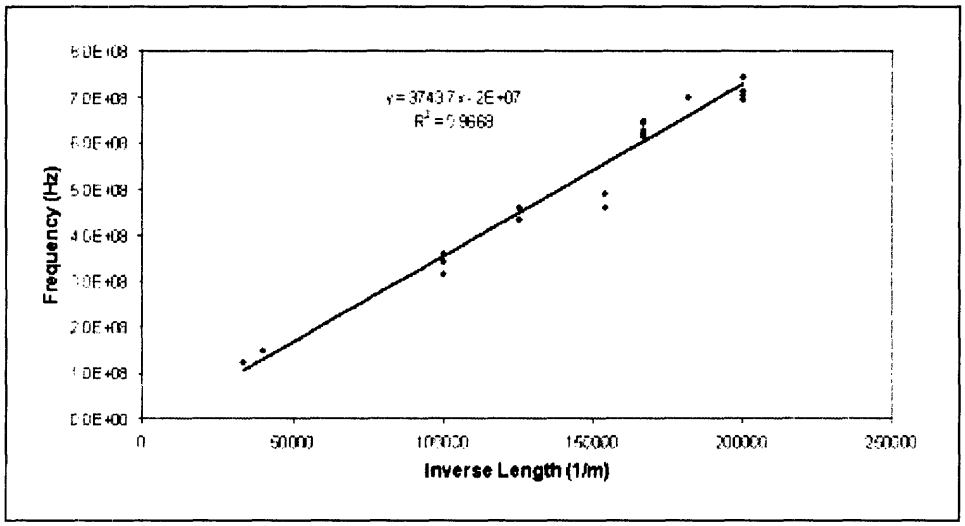

Figure 1.7: Frequency vs. inverse length for previously measured resonators.[1]

As the size of the resonator decreases, other features such as the tether width also decrease accordingly. Feature sizes less than 0.5-1 μm cannot be easily replicated with conventional contact lithography methods, primarily due to diffraction and non-intimate mask to wafer contact. Therefore, conformable contact lithography (CCL) is utilized to produce the smallest feature sizes and hence increase resonator frequency. Sloped sidewalls also limit the feature size of the resonator and tethers since the cross-sectional shape degrades as the desired feature size is decreased. Figure 1.8 compares the cross section of a 2 μm tether to a 0.3 μm tether, each with a sidewall angle of 60°. It is apparent that the sidewall angle degrades the intended cross-sectional shape as the feature size is decreased. More importantly, the sidewall angle restricts the minimum feature size to 0.58 μm. Thus, a Cl-based dry etch producing straighter sidewalls is needed in order to reduce feature sizes and increase resonator frequency.

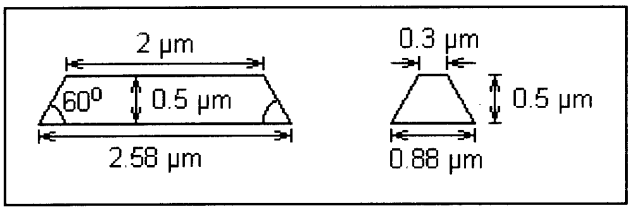

Figure 1.8: Cross-sections of 2 μm and 0.3 μm features with a sidewall angle of 60°.

1.5 New Resonator/Mask Design

Previous device measurements have shown that better performance characteristics are obtained by connecting the resonator to the tethers along its width (i.e. non-resonating) dimension (see Figure 1.9). The most recent resonator design uses this orientation as well as notched attachment points at the tether-resonator interface (see Figure 1.9).

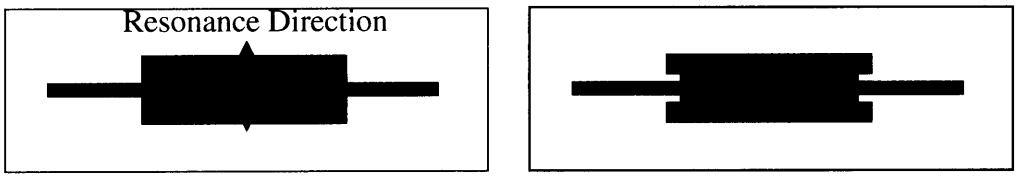

Figure 1.8: Left – Resonator connected along it width dimension showing resonance direction of interest; **Right** – Resonator with notched attachments.

The inclusion of notched attachment points allow support beams (tethers) to attach closer to the resonator's actual nodal points [8]. This reduces acoustic losses through the support beams by reducing the interference between supports and the natural mode shape of the resonator [9]. Ring resonators utilizing notched attachment points have been shown to more than double the Q values of their un-notched counterparts [8] and produce cleaner electrical signals [9]. The new design also increases the resonator size (areas of 50-300 μm^2) by increasing the width (non-resonating) dimension. This change was made since no signal was obtained for smaller area devices from previous fabrications.

1.6 New Fabrication Process

Figure 1.10 presents a schematic representation of the new fabrication process flow.

- The new resonator fabrication process begins with same initial stack of materials as the old fabrication process (Si, SiO_2, "seed" AlN, Mo, AlN). Next, 1500 Å of Cr and 4000 Å of SiO_2 are deposited on the stack. The SiO_2 is patterned by reactive ion etching (RIE) in fluorine-based plasma and serves as an etch mask.
- Next, a Cl-based electron cyclotron resonance (ECR) etch of the "stack" (Cr, AlN, Mo, and "seed" AlN) is made, forming the shape of the resonator, tethers, and one bond pad.
- The bottom metal of that bond pad is then exposed by removing the Cr and AlN with a Cl-based ECR etch.
- Next, both bond pads are patterned with a liftoff of chrome (Cr), platinum (Pt), and gold (Au).
- Finally, a precisely aligned, timed release etch in buffered hydrofluoric acid (BHF) is completed.

The new fabrication process should yield smaller feature sizes and eliminate the free-hanging ledge at the bond pads. These improved fabrication results are expected to improve the Q and frequency range of the resonator.

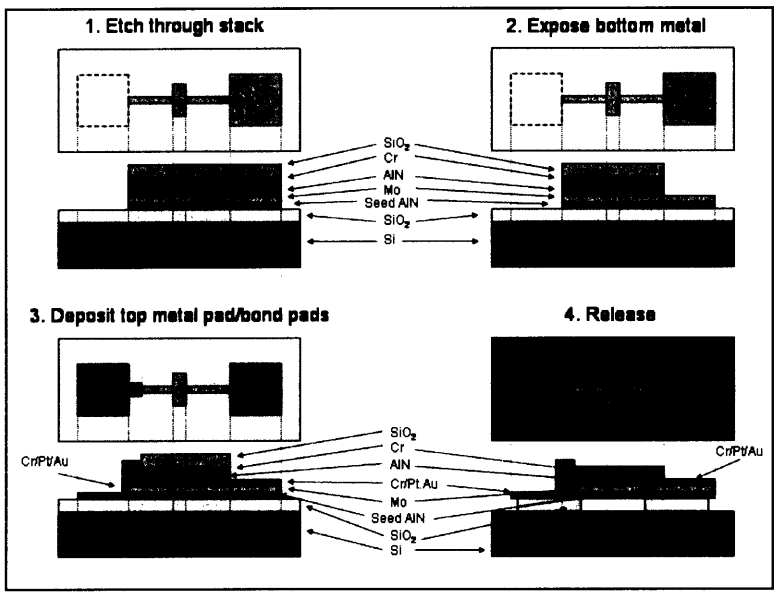

Figure 1.10: New fabrication process flow.[1]

Chapter 2
Conformable-Contact Lithography (CCL) and Moiré Alignment

Conformable-contact photolithography (CCL) with moiré-based alignment has demonstrated a mean alignment accuracy of less than 35 nm with an uncertainty of pattern overlay of less than 60 nm (for a 30 mm x 30 mm area) in multi-level patterning experiments [10]. The alignment marks used were gratings consisting of equispaced concentric circles which create highly sensitive optical moiré patterns. A single mask was used for the experiment. The alignment accuracy reported in [10] is for a single, manually aligned mark and therefore larger alignment errors can be expected when a pair of marks is considered. In addition, the pattern placement accuracy for a typical fabrication process is likely to be far worse than what is reported in [10] since it was determined for a small area (30 mm x 30 mm). Furthermore, a typical multi-level alignment process will utilize multiple masks which will also increase the alignment and pattern placement error. It seems unlikely that the level of alignment and pattern placement accuracy reported in [10] can be readily achieved in a typical fabrication process due to the controlled conditions of the experiment. However, CCL with moiré based alignment is still expected to yield better alignment accuracies than a typical contact photolithography process.

As discussed in chapter 1, the CCL process aids in producing the smallest features (0.5 μm) with high yield on the new L-bar mask design and holds the potential for producing even smaller features in future device fabrications. The moiré alignment process is needed in order to perform an aligned released which will eliminate the free hanging ledge at the bond pad and in theory increase the Q of the device. An automated alignment system using image analysis software was also developed in order to simplify the alignment process and have the alignments eventually performed by technicians in the Draper cleanroom. This section discusses conformable-contact lithography, moiré

alignment, the automated alignment design, and an alignment experiment employing the two techniques.

2.1 Conformable-Contact Lithography

2.1.1 Contact Lithography Limitations

Contact photolithography involves bringing a mask into contact or near proximity with a substrate to be patterned. In this lithography process the resolution and quality of the pattern transfer is limited by a variety of factors. These factors include the diffraction of the light as it passes through a transparent area in the mask, wafer flatness, and debris between the substrate and mask. Figure 2.1 shows the light distribution on a photoresist surface after passing through a mask with a periodic grating of opaque and transparent spaces of equal width. Since there is a gap between the mask and wafer, the light transfer is not ideal. In addition, the pattern fidelity is further diminished by the diffraction of light as it passes through the resist.

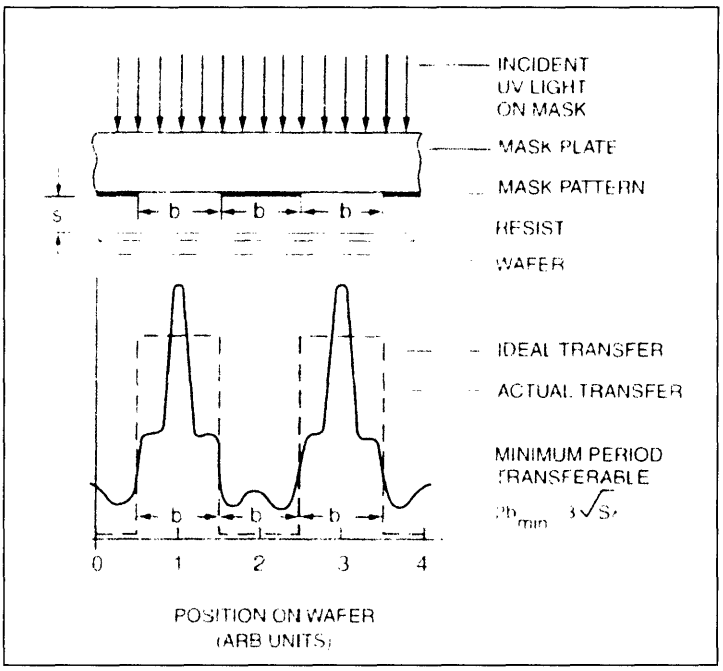

FIGURE 2.1: Light distribution on a photoresist surface after passing through a mask of equispaced transparent gratings [11].

Diffraction effects as illustrated in Figure 2.1 cause a perfectly clean edge to become blurred or skewed. Assuming that diffraction is the only limiting factor, the resolution in contact and proximity photolithography can be theoretically determined by the equation below [11].

$$R = b_{\min} = \frac{3}{2}\sqrt{\lambda\left(s + \frac{z}{2}\right)} \tag{2.1.1}$$

where b_{min} = half the grating period and the minimum feature size transferable, s = gap between the mask and the photoresist surface, λ = wavelength of the exposing radiation, and z = photoresist thickness. For a contact photolithography process, the two variables that would affect the resolution are the wavelength of the exposing radiation and the photoresist thickness. From the above equation, it is clear that in order to achieve a higher resolution shorter wavelengths and thinner resists are needed. Assuming a wavelength of 400 nm and a resist thickness of 200 nm, a resolution of 300 nm is projected. In practice, theoretical resolutions based on (2.1.1) are rarely achieved due to

variable gaps and diffractions that can be attributed to wafer nonflatness and particles between the mask and the substrate. In order to mitigate this problem, conformable contact lithography (CCL) utilizes flexible masks that conform to variations in substrate surfaces. A comparison of a conventional mask and a flex mask with a particle between the mask and substrate is depicted in Figures 2.2 and 2.3.

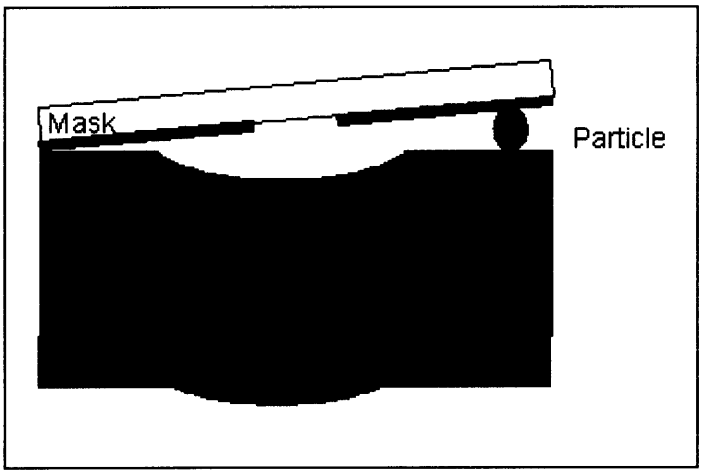

Figure 2.2: Particles and wafer nonflatness cause variable gaps and variable diffraction in a conventional mask.[1]

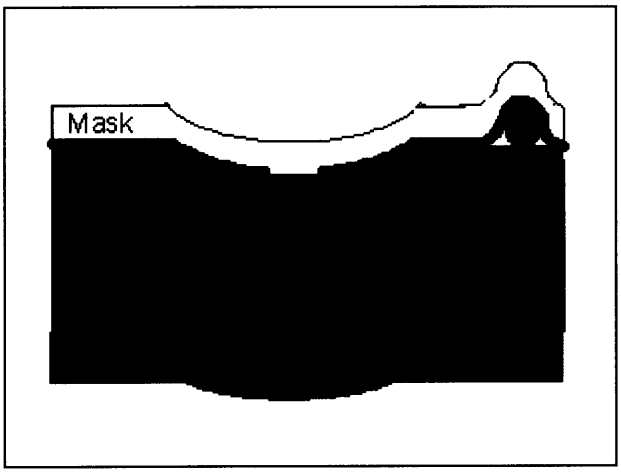

Figure 2.3: A flex mask is able to conform around substrate shape variations.[1]

[1] Figure(s) courtesy of Dr. David J. Carter, MEMS Group, Draper Laboratory

Conformable flex masks have been used as far back as 1969 to pattern micron-level feature sizes [12]. There are several different contact lithography methods that appear capable of sub-100 nm patterns. Some of these methods are categorized as "soft lithography" and utilize highly elastic polymeric masks. These methods are not diffraction limited, are very accommodating to rough surfaces, and are low-cost since the polymers that the masks are constructed from are widely available on the commercial market [13]. However, they are limited by the "intrinsic structure-forming capability of elastomers and by the effects of distortion during the printing process" [13]. The pattern placement accuracy in "soft lithography" has been limited to approximately 0.5 μm over a 1 cm^2 area [14]. These limitations pose a problem to multi-level patterning applications such as the Draper MEMS Resonator. The flex mask used in the Draper CCL process consists of a 100 mm diameter by 0.5 mm thick UV-grade fused silica wafer bonded to a 127 mm outer diameter by 10 mm thick Pyrex ring. Chrome is patterned on the mask by evaporation and liftoff.

2.1.2 Conformable-Contact Lithography System Layout

The equipment that was used to perform CCL was the LiLCo Systems CCA-M4 Conformable Contact Aligner (LiLCo Systems, Melrose, MA)[2]. The major components of the system are the aligner head, dual-microscope head, main chassis, and remote console. The layout of the system is shown in Figure 2.4.

[2] Details of the following system description were taken from the LiLCo Systems CCA-M4 Conformable Contact Aligner Owner's Manual.

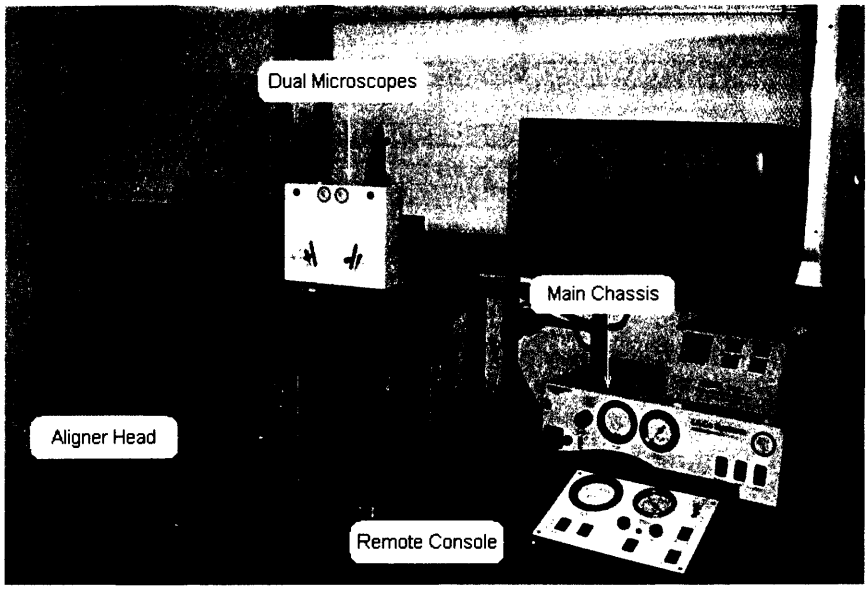

FIGURE 2.4: CCL system layout.[1]

The aligner head sits on the vibration-dampened workstation's main table and is powered by a pneumatic cylinder that allows it to slide from the center to the left side of the table along rails. It also holds the mask-holding plate, substrate-holding chuck, and the X, Y, θ (rotational), and Z substrate adjustment mechanisms. The mask-holding plate has a manual three-point leveling system with a mask tilt precision of approximately 0.63 mrad. The substrate-holding chuck is flat to less than 0.0005". The original X, Y, θ, and Z adjustments operated with manual micrometers were replaced with piezo-actuators. Each of the X and Y substrate adjustments are now composed of sliding stages that can be moved with either a crude manual micrometer or a Polytech PI P-841.30 piezo-actuator. The θ adjustment is similar to the X and Y adjustments except that the micrometer and piezo-actuator move a rotational stage. The piezo-actuators have a range of travel of 45 μm and sub-nanometer resolution. The Z adjustment mechanism is a Polytech PI M-501.1 DG motorized vertical positioning stage. The vertical positioning stage has a travel range of 12.5 mm and a minimum incremental motion of less than 0.1 μm. These components were installed so that a computer image analysis alignment system could be employed.

The dual microscope head rests on rails above the main table and is moved front and back by a pneumatic cylinder. The microscopes are used to view two alignment marks simultaneously. The microscope head can be precisely moved in the X and Y directions by micrometers located behind the microscopes. Both microscopes have a field of view of 300 μm and internal illuminations of 590 nm wavelengths.

2.1.3 Conformable-Contact Lithography Procedures

The first step in performing a CCL aligned printing is to blow dry, filtered air over the substrate chuck, substrate, and mask to clean off as many particles as possible. The mask will conform around particles, but ultimately the presence of particles, depending on their size, degrade the replication pattern or possibly cause damage to the mask. Particles between the mask and the wafer will cause certain areas to be out of contact. These areas are easily identified with the naked eye by interference rings as illustrated in Figure 2.5.

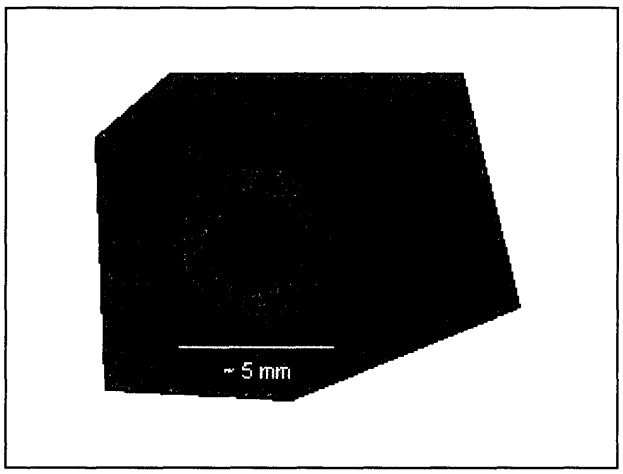

Figure 2.5: Illustration of interference rings caused by a particle between the mask and substrate. The number of rings depends upon the size of the particle.

After removing as many particles as possible, the substrate is placed on the substrate chuck and secured using the substrate chuck vacuum. The flex mask is then put into place with the pattern facing down in the mask holding plate and secured with retaining clips. Contact vacuum is applied after the wafer is brought to within close proximity of

the mask. Next, the vacuum is released, alignment corrections are made, and contact vacuum is reapplied. After the mask and substrate are brought into alignment, the substrate is exposed.

2.2 Moiré Alignment Theory

Conventional alignment marks consist of a cross-in-box configuration as shown in Figure 2.6. The sensitivity to misalignment of these marks is limited by the image resolution and the operator's visual acuity. Typical alignment overlay accuracies using conventional contact lithography and conventional alignment marks at the Draper MEMS fab are on the order of 1-2 μm [5]. Far more accurate alignments can be achieved by utilizing moiré interference patterns which greatly enhance the sensitivity to misalignment. Conformable-contact photolithography (CCL) with moiré-based alignment has demonstrated a mean alignment accuracy of less than 35 nm with an uncertainty of pattern overlay of less than 60 nm in multi-level patterning experiments [10]. The alignment marks used in the CCL process were equispaced circular gratings as shown in Figure 2.7 (this method was first used in the 1970s and at the time predicted alignment accuracies of less than 100 nm after technological advances) [15].

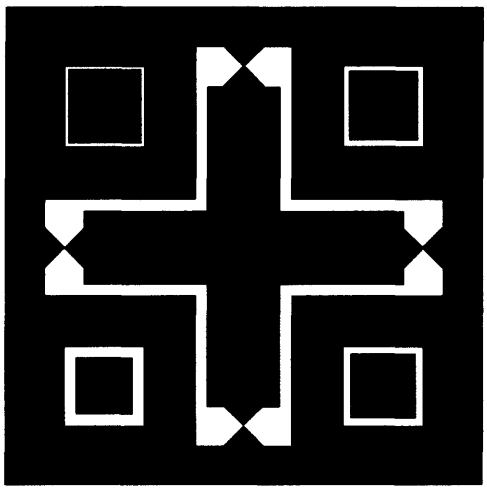

Figure 2.6: Conventional cross-in-box alignment marks.

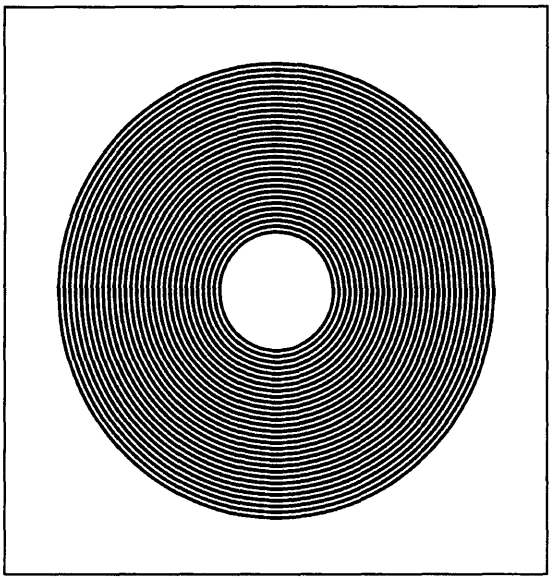

Figure 2.7: An alignment mark consisting of equispaced concentric circles.

When the gratings on the mask are put over the gratings on the substrate, an optical interference or moiré fringe pattern is produced [10]. The moiré pattern is caused by the beating of the two gratings on the mask and wafer. This alignment technique is highly sensitive to misalignments and provides the operator with qualitative and quantitative information so that alignment can be achieved [15]. When the gratings on the mask and wafer are of the same pitch, the misalignment between the two gratings is equal to the number of fringes passing through the center or the gratings multiplied by one-half the pitch [15]. In Figure 2.8, the gratings have a cut-out center portion similar to a doughnut. If there was no empty center portion, it would be clear that 4 fringes are passing through the center of the gratings. Nevertheless, it can be inferred in Figure 2.8 that 4 fringes are passing through the center and since the pitch of the gratings is 2 μm, the misalignment is 4 μm.

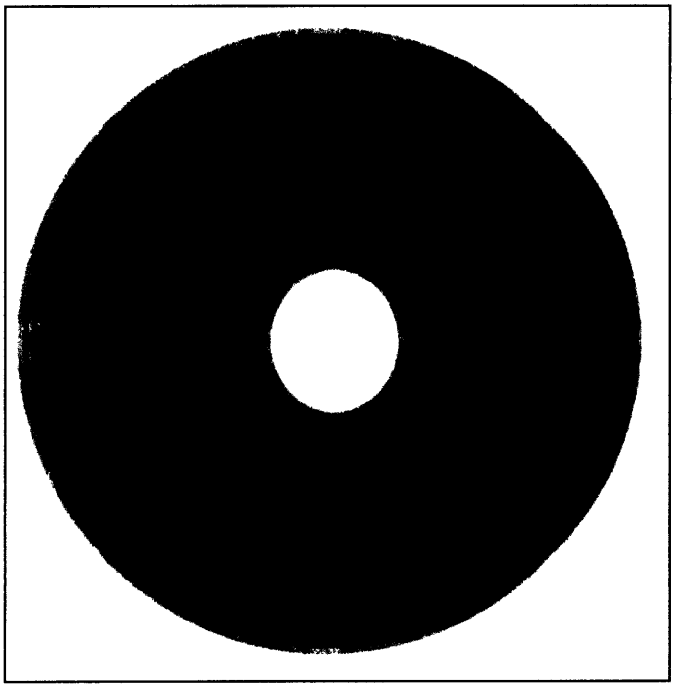

Figure 2.8: Simulated misalignment with marks of equally-pitched circular gratings. The pitch of the gratings is 2 μm, thus it can be inferred from the image that there is a misalignment of about 4 μm.

The problem with having gratings of the same pitch is that when perfect alignment is achieved there is no moiré pattern, thus the accuracy is limited to one-half the pitch of the gratings [15]. This problem is solved by setting the pitch on one set of the gratings slightly larger than the other. Under this condition, circular moiré fringes are produced at perfect alignment. The mathematical characterization of the moiré fringes given below has been previously discussed in various publications including [15] and [16]. Two gratings of the same pitch can be described by the following equations.

$$(x-s)^2 + y^2 = n^2 a^2 \tag{2.2.1}$$

$$(x+s)^2 + y^2 = k^2 a^2 \tag{2.2.2}$$

where s = one-half the misalignment, n = some integer, k = some integer, and a = pitch. A moiré pattern will be created by the loci connecting the points of intersection of the two gratings that comply with the equation

$$p = n \pm k \tag{2.2.3}$$

where p = any integer. Solving for (2.2.1), (2.2.2), and (2.2.3) yields

$$\frac{x^2}{\left(\frac{p^2}{4}\right)} \pm \left\{ \frac{y^2}{\left[\frac{p^2}{(4-s)}\right]} \right\} = 1 \tag{2.2.4}$$

which describes a series of ellipses and hyperbolas. If gratings of different pitch are now taken into consideration and assuming perfect alignment, (2.2.1), (2.2.2), and (2.2.3) yield

$$x^2 + y^2 = \left[\frac{(p + \frac{1}{2}) p_a p_b}{(p_a - p_b)} \right]^2 \tag{2.2.5}$$

where p_a and p_b are the pitches of the two gratings. The pitch of the circular moiré pattern produced by two different gratings is given by the following equation.

$$p_m = \frac{p_a p_b}{|(p_a - p_b)|} \tag{2.2.6}$$

It is worth noting that it is not necessary to be able to resolve the individual lines of the gratings since the moiré fringe pattern is easily seen when two gratings are overlapped. If the moiré period p_m is equal to n pitch widths then

$$p_m = n p_a \tag{2.2.7}$$

The accuracy or sensitivity to misalignment is then

$$Accuracy = \pm\left[\frac{\left(p_a/2\right)}{n}\right] \tag{2.2.8}$$

Combining (2.2.6), (2.2.7), and (2.2.8) yields

$$Accuracy = \pm\left(\frac{p_a}{2}\right)\left[\frac{\left|\frac{p_b}{p_a} - 1\right|}{\left(\frac{p_b}{p_a}\right)}\right] \tag{2.2.9}$$

Therefore, sensitivity to misalignment can be increased in three ways: The first is by reducing the pitch of the gratings while keeping the difference between the two pitch widths the same. This has a limited effect. The second is to decrease the difference between the two pitch widths while keeping p_a the same. This method has a much greater effect. However, this also increases the moiré period and therefore is of no use once the radius of the moiré fringe approaches the radius of the marks. The third and most efficient way is to decrease the pitch of the gratings while keeping the ratio between them the same. This increases the sensitivity to misalignment while maintaining the placement of the moiré period in relation to the radius of the marks.

If the pitch of the gratings is known, the alignment error can be easily approximated by observing the location of the first fringe. When the first fringe is decentered a distance equal to its radius, the gratings are misaligned by one-half the pitch width of the smaller pitch. As the alignment error increases, the fringe that forms on the interior of the first fringe aids in determining the misalignment. When this second fringe is located where the first fringe would be if perfectly centered, then the gratings are misaligned by one pitch width. Figure 2.9 show simulations of gratings that are centered, misaligned by one-half a pitch width, and misaligned by one pitch width respectively.

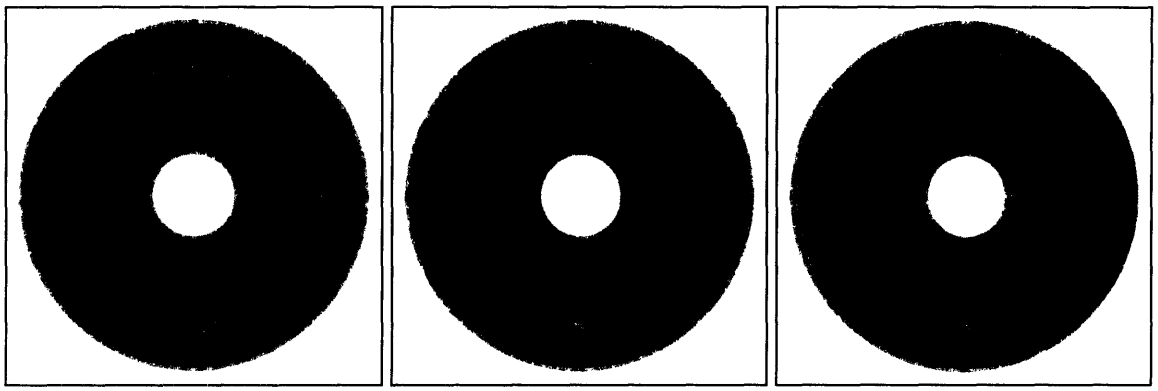

Figure 2.9: Left – Centered gratings; **Middle –** Gratings misaligned by one-half pitch width; **Right –** Gratings misaligned by one pitch width.

The direction that the gratings are misaligned is also easily determined. The "spider" formation that the gratings produce are intuitive to the operator since you simply move the grating with the smaller pitch in the direction that the spider is pointed. For example, if the pitch on the substrate in Figure 2.9 (right) is smaller than that on the mask, you would move the substrate to the left.

2.3 Computer Image Analysis

The goal of the alignment process was to automate the procedure so that a skilled technician could perform alignments with minimal involvement. The conceived plan was to have the operator manually perform a rough alignment, snap images of the roughly aligned marks, and then have computer image analysis software determine the misalignment and correct it automatically. All analysis done in the following sections was performed with National Instruments Labview 7.1 and Vision 7.1. Prior to doing experiments with real alignment marks, alignment simulations were run to determine the theoretical accuracy of the alignment algorithm for a single pair of marks.

The assumption when starting the alignment simulations was that the operator would be able to manually align the marks with the manual micrometers to less than one-half the pitch width, such that the first circular fringe would still be encapsulating the white center

of the marks. A "fine alignment" algorithm was then written to correct this misalignment. The issues that needed to be addressed for this algorithm were locating the moiré fringe, locating the centroid of the alignment marks, and correctly realigning the marks. A "coarse alignment" algorithm was also written to roughly align the gratings to less than one-half the pitch in the case where the operator was unable to do this.

2.3.1 Moiré Fringe Location

The basis for the "fine" alignment algorithm was determining the relative displacement of the circular moiré fringe in relation to the centroid of the gratings (both of which have radial symmetry). For the purpose of illustration, an algorithm that determines the distance that a solid black circle is moved from its center point is described.

The algorithm utilizes a Labview function that finds the pixel intensity values along a line. Radial line scans at one-degree increments were made from a starting center point and a 200 pixel diameter black circle was randomly moved up to ±50 pixels in the x and y directions. Figure 2.10 shows a diagram of a non-centered circle and measurements taken from the starting center point to the edge of the circle at 0, 90, 180, and 270 degrees. The distances from the starting center point to the edge of the circle was determined and plotted versus the angle (0^{o}-360^{o}) at which the distance was measured. If the circle is moved from the center, the resulting plot is a sine/cosine wave. A best fit cosine was then plotted against the measured data. The cosine function was arbitrarily chosen for the model since either the sine or cosine function could have been used. The general form of any cosine function is

$$y = a * \cos[b(x + c)] + d \tag{2.3.1}$$

where a affects the amplitude, b affects the period, c affects the phase shift, and d affects the vertical shift. For the experiment discussed earlier

$$a = \frac{(D_{max} - D_{min})}{2} \tag{2.3.2}$$

$$b = \frac{2\pi}{360} \tag{2.3.3}$$

$$c = \theta_{@\, D_{max} / D_{min}} \tag{2.3.4}$$

$$d = \frac{(D_{max} + D_{min})}{2} \tag{2.3.5}$$

where D_{max} = maximum distance from original center to edge of circle and D_{min} = minimum distance from original center to edge of circle. Figure 2.11 illustrates the sine/cosine wave that is produced when R (the distance from the starting center point to the edge of the circle) is plotted versus θ (angle in degrees from which the distance was determined).

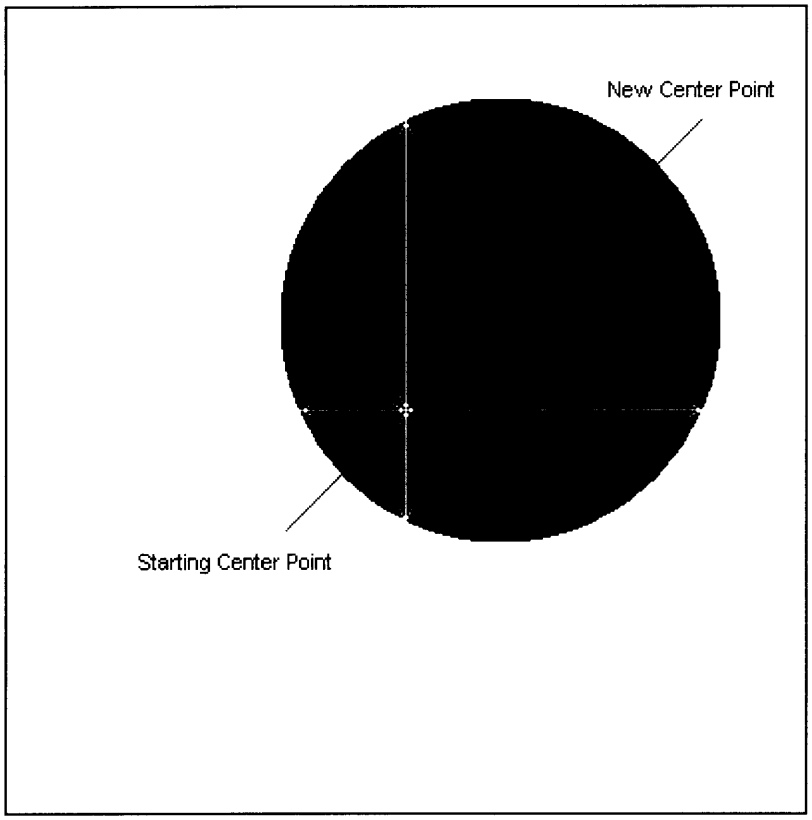

Figure 2.10: Measurements are taken from the original center of the circle prior to moving it, to the edges of the new circle. The result of these distances is a sine/cosine wave.

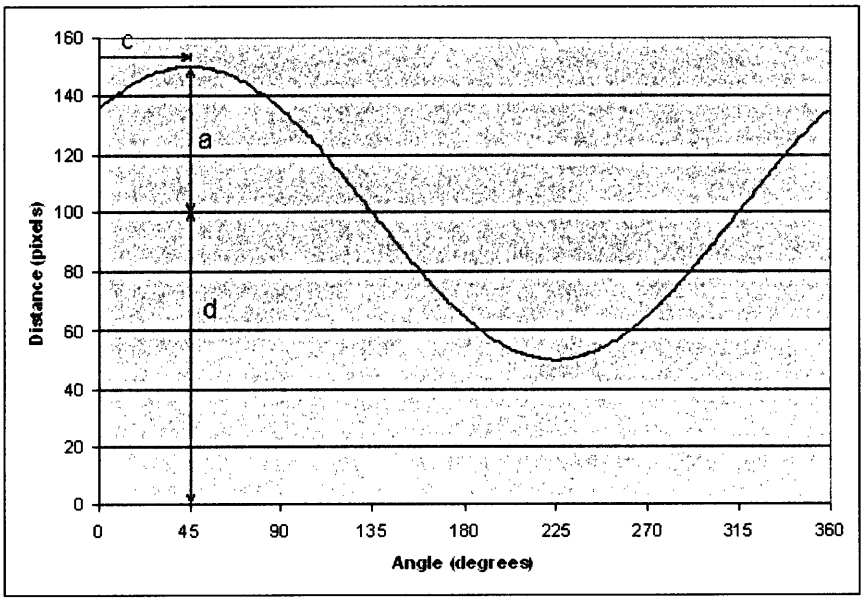

Figure 2.11: Cosine wave from 200 pixel radius circle shifted 50 pixels at 45°.

The distances that the circle was moved in the x and y directions were then easily determined using simple trigonometry.

$$x = \cos(c) * a \tag{2.3.6}$$

$$y = \sin(c) * a \tag{2.3.7}$$

2.3.2 Centroid Location

A source of error that was to be expected was finding the location of the centroid of the overlapped alignment marks. A simulation was run that misaligned a pair of marks by up to one-half a pitch width and moved the marks to a random location within the image window. The Labview IMAQ Count Objects function was used to locate the centroid of the marks. This function locates the centroid of objects that fall within the user given parameters such as size and pixel intensity. The results of 1000 measurements are shown in Table 2.1.

Table 2.1: Centroid Location Error (in pixels).

$\mu_{Error\ X}$	-0.001
$\mu_{Error\ Y}$	0.001
σ_X	0.041
σ_Y	0.043

It is also important to note that the centroid of the marks is not the true center (center of the mark on the mask), but actually half-way between the center of the marks on the substrate and the mask. This is illustrated in Figure 2.12.

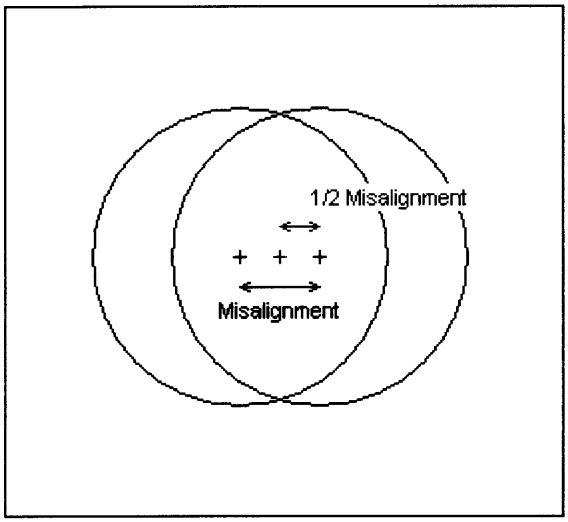

Figure 2.12: Centroid location of misaligned marks.

2.3.3 Shift Factor

After determining the accuracy of finding the centroid of a set of alignment marks, an algorithm for the "fine alignment" was written to find a circular moiré fringe, determine its offset, and then apply the necessary corrections to align the marks. For this operation, a shift factor was needed since the decentered distance of the moiré fringe compared to the misalignment is not a one to one ratio. As stated earlier, when the first fringe is decentered a distance equal to its radius, the gratings are misaligned by one-half their pitch width. Applying this to (2.2.6), the following ratio can be made of fringe displacement to substrate displacement

$$\frac{1}{2}\left(\frac{p_a p_b}{|(p_a - p_b)|}\right) : \frac{1}{2} p_a \tag{2.3.8}$$

Now accounting for the fact that the distance from the centroid of the two marks to the fringe is one-half the misalignment subtracted from the distance from true center to the fringe

$$\frac{1}{2}\left(\frac{p_a p_b}{|(p_a - p_b)|}\right) - \frac{1}{2}m : \frac{1}{2}p_a \tag{2.3.9}$$

where m = the misalignment. Since the misalignment is one-half the pitch width for the given case

$$\frac{1}{2}\left(\frac{p_a p_b}{|(p_a - p_b)|}\right) - \frac{1}{4}p_a : \frac{1}{2}p_a \tag{2.3.10}$$

After dividing by one-half the pitch width the following ratio of fringe displacement to substrate displacement is created

$$\left(\frac{p_b}{|(p_a - p_b)|}\right) - \frac{1}{2} : 1 \tag{2.3.11}$$

This ratio is used to scale the fringe displacement to the substrate displacement. With the exception of Mark 3 in Table 2.2, this "shift ratio" is 20.5:1 (in pixels). This means that for every 20.5 pixels that the moiré fringe is displaced the substrate is displaced by 1 pixel. For "real world" alignments, the fringe displacement (in pixels) needs to be converted to a substrate displacement (in μm). Therefore, the resolution of the captured images will affect the "shift ratio". For example, if the image resolution were such that 1 pixel = 0.1 μm, then the "shift ratio" would increase by a factor of 10.

2.4 Alignment Simulation

A Labview program was constructed that simulated the sequence of events similar to an actual alignment scenario. First, the user is able to determine which set of alignment marks would be used for the alignment. The figure and table below presents the specifications of each of the marks. "Mark 1b" was laid over "Mark 1a", "Mark 2b" over

"Mark 2a" and so forth. These marks were selected since they were already on existing alignment test masks.

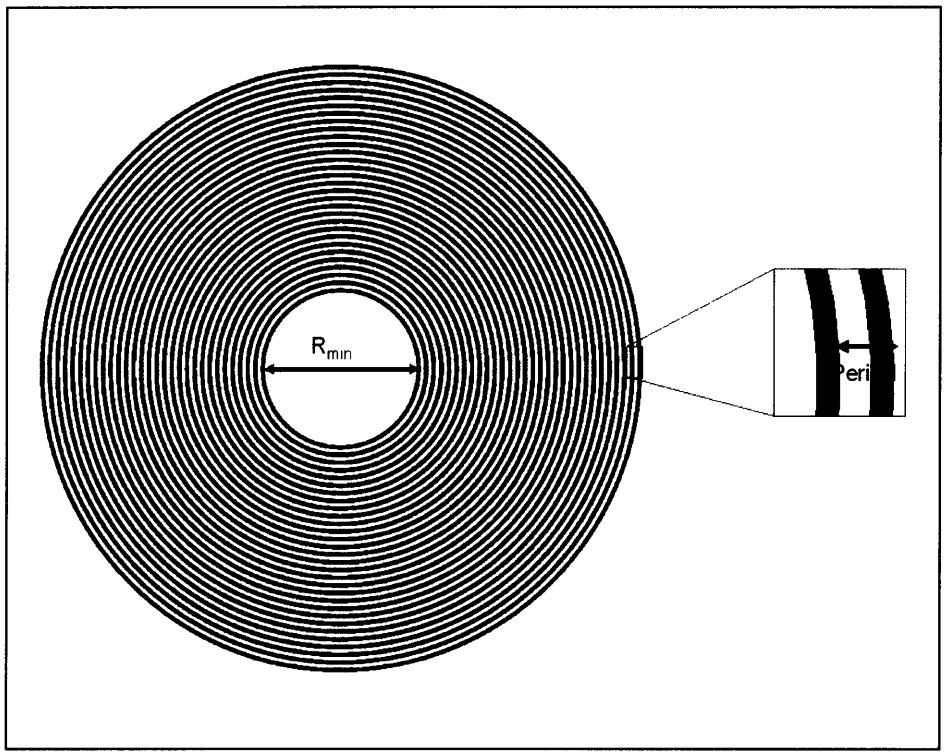

Figure 2.13: Mark definitions.[1]

Table 2.2: Mark descriptions.[1]

Mark Name	Rmin(um)	Period (um)	# cycles
1a	20	2	30
1b	20	2.1	30
2a	20	2	50
2b	20	2.1	50
3a	20	2	50
3b	20	2.05	50
4a	20	2	30
4b	20.25	2.1	30
5a	20	2	30
5b	20.5	2.1	30
6a	20	2	30
6b	21.5	2.1	30
7a	20	2	30
7b	21	2.1	30
8a	20	2	40
8b	20.25	2.1	40

Next, the corresponding pair of marks is randomly misaligned by up to a pitch width in the x and y directions and moved to a random location within the image window. The image is then scaled to a resolution of 400 pixels by 400 pixels. This resolution was selected since it closely matches the real image resolution of 640 pixels by 480 pixels. The user then selects whether a "coarse" realignment or a "fine" realignment is to be conducted depending upon the severity of the misalignment. The "coarse alignment" algorithm is designed to get the marks aligned close enough so that the "fine alignment" can accurately correct the misalignment. This algorithm requires the user to draw a line parallel to the front of the "spider" and input the number of fringes that are passing through the center point (see Figure 2.15). This information provides the direction in

which to move the mark and the number of half-pitch widths. After the "coarse alignment" is performed (if it is needed), a "fine" realignment is done depending on the user input. Finally, the aligned image is displayed along with the accuracy of the alignment.

Figures 2.14-2.17 represent the simulated alignment sequence in Labview. The marks are misaligned by roughly one pitch width. The upper graph located in Figure 2.17 is a plot of pixel intensity versus distance from the centroid for each intensity reading taken at 1^{o} increments. The lower graph in Figure 2.17 is a plot of the distance from the centroid to the fringe versus the angle that the distance is measured at. The best fit cosine wave is plotted in white over the measured data points which are in red.

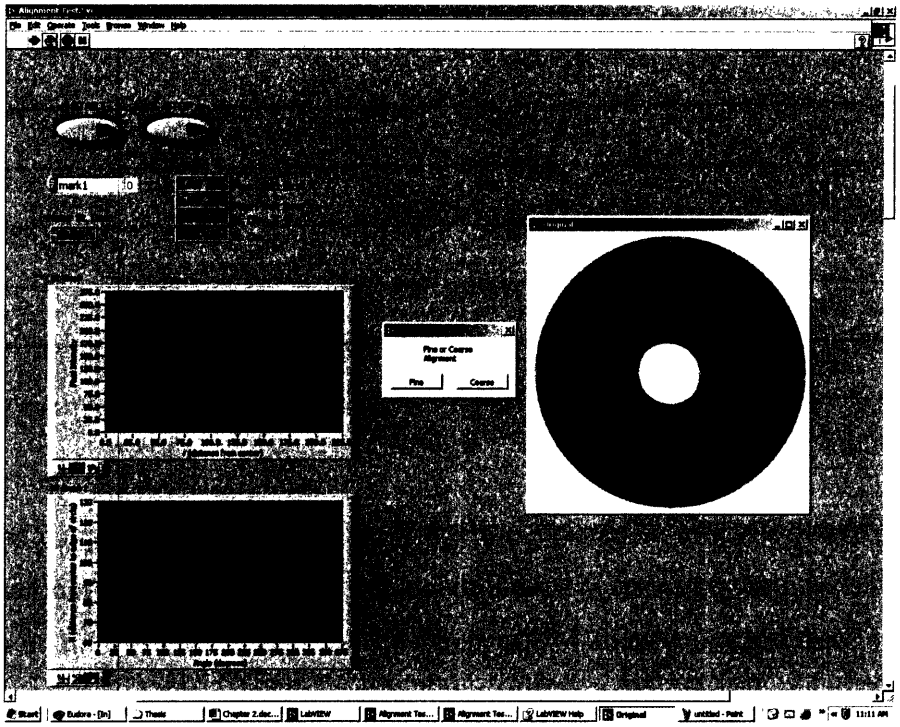

Figure 2.14: Marks misaligned by ~ 1 pitch width. The operator selects Fine or Coarse Alignment.

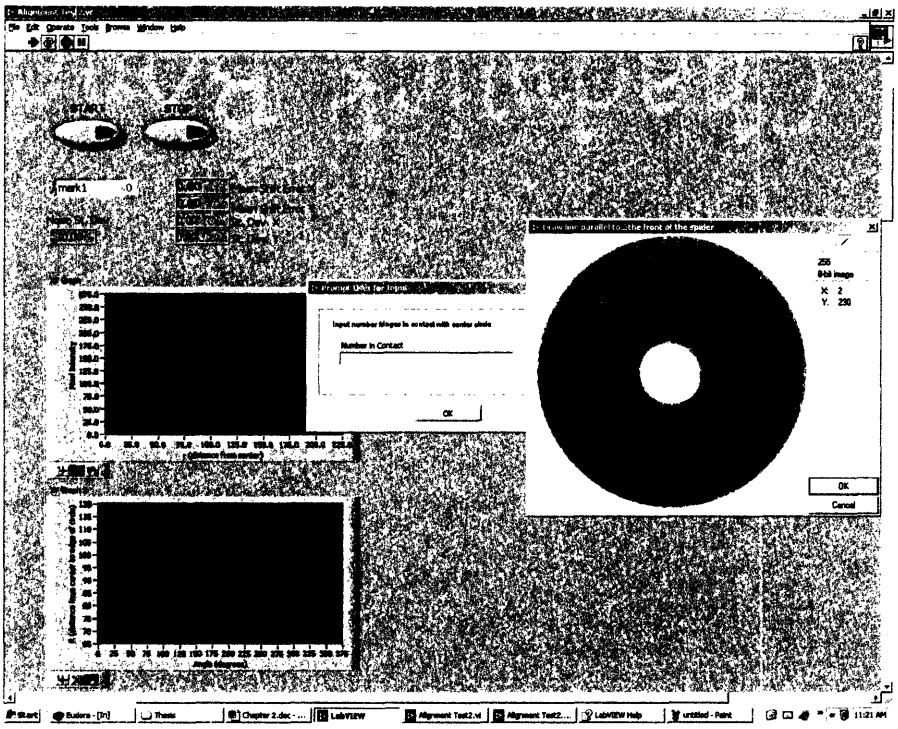

Figure 2.15: The operator draws a line parallel to front of "spider" and inputs "2" as the number of dark fringes passing through the center point.

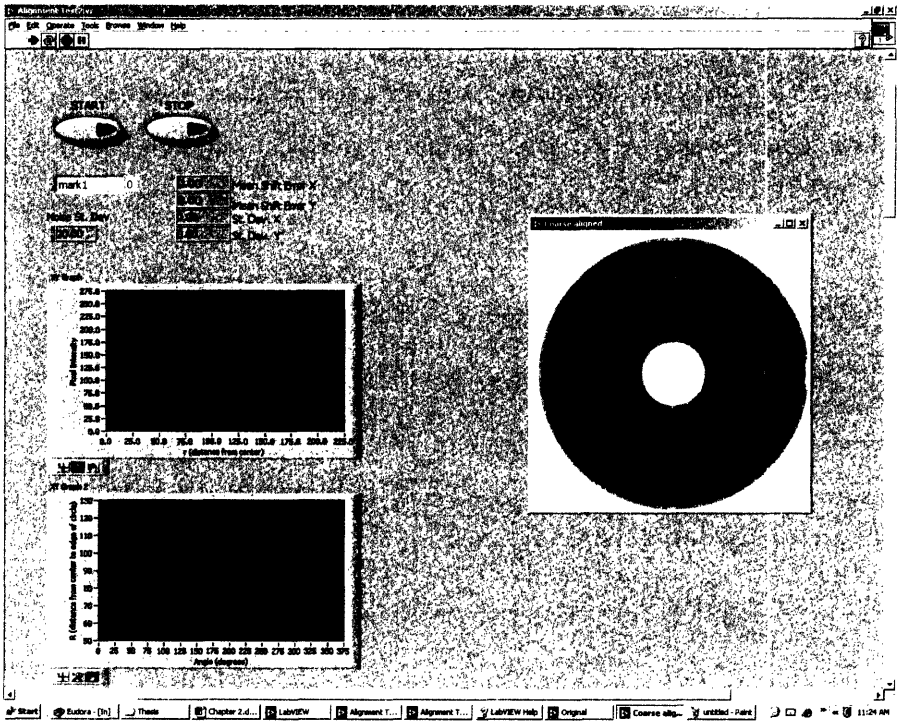

Figure 2.16: The marks are now coarsely aligned based upon the operator's inputs. The automated algorithm will now perform the "fine" alignment.

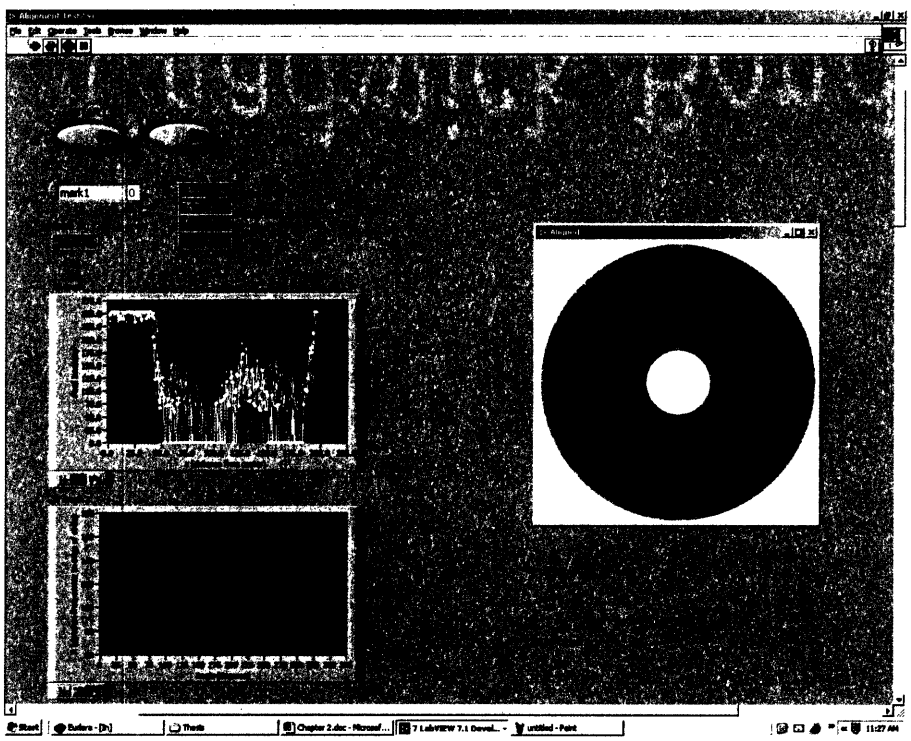

Figure 2.17: The marks are automatically aligned. In this example, there is an alignment error of 0.27 pixels in the x direction and 0.26 pixels in the y direction.

For the particular alignment sequence shown above in Figures 2.14-2.17, the marks are misaligned by 0.27 pixels in the x direction and 0.26 pixels in the y direction. The mean accuracy and standard deviation of 100 alignment sequences is shown below in Table 2.3.

Table 2.3: Alignment accuracy simulation results (in pixels).

$\mu_{\text{AlignError X}}$	0.002
$\mu_{\text{AlignError Y}}$	0.001
σ_X	0.063
σ_Y	0.058

Table 2.4 contains the predicted automated alignment accuracy mean and confidence intervals based upon the simulated images resolution and the pitch widths of the alignment marks (1 pixel $\approx$ 0.5 μm).

Table 2.4: Predicted automated alignment accuracy.

	X	Y
$\mu_{AlignError}$	~0.98 nm	~0.40 nm
68% within	~30 nm	~30 nm
95% within	~60 nm	~60 nm
99% within	~90 nm	~90 nm

2.5 Experimental Alignment Issues

When performing a real alignment, other issues exist that were not addressed in the alignment simulation. One set of issues is theoretically expected while the other is the result of system noise. The theoretical issues are rotational alignment and magnification error. The system noise issues are the image fidelity of the real marks, contact and release repeatability, and commanded versus actual movements.

2.5.1 Rotational Alignment

In the actual alignment, two marks located on opposite locations on a mask are used in order to achieve rotational alignment. The LiLCo Contact Aligner is designed for viewing alignment marks located on the left and right side of the mask. Assuming that the alignment marks on the substrate are perfectly centered on the wafer chuck, a rotational movement will cause the marks to move equal distances, but in opposite directions of each other.

However, it is highly unlikely that an operator will be able to perfectly center the marks on the wafer on the wafer chuck. Thus, the misalignment of the marks on the wafer in relation to the wafer chuck's center of rotation must be accounted for when performing a rotational movement of the alignment marks. An algorithm for determining this

misalignment is presented below. Figure 2.18 depicts the relationship between the wafer chuck's center of rotation and the right alignment mark before and after a counterclockwise rotation.

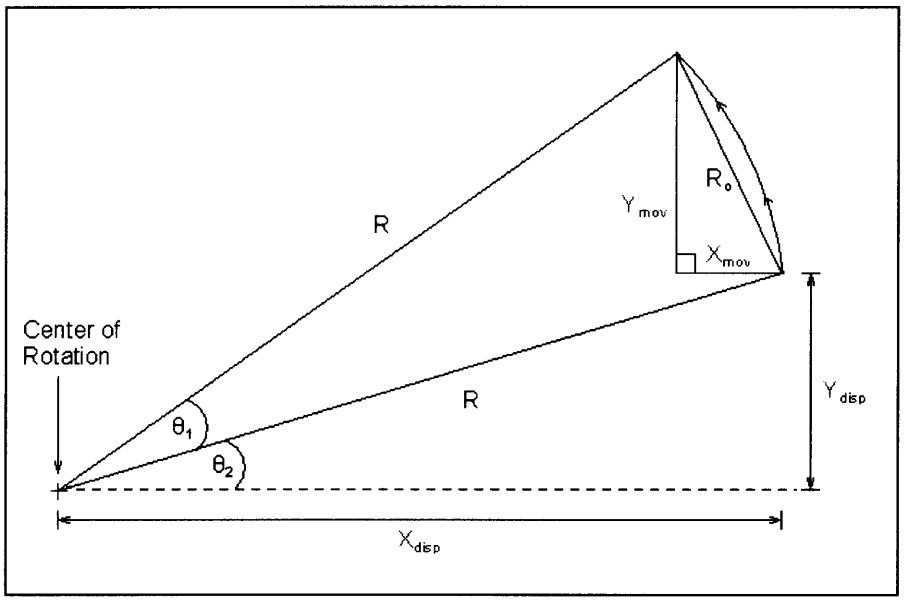

Figure 2.18: Wafer chuck center of rotation in relation to a mark on the wafer.

If you assume that the chord length R_o is equal to the arc length for extremely small angles and $\theta_2 < \pi/4$ rads

$$R_o = 2R\sin(\theta_1/2) \tag{2.5.1}$$

$$X_{mov} = R_o \sin(\theta_2) \tag{2.5.2}$$

$$Y_{mov} = R_o \cos(\theta_2) \tag{2.5.3}$$

$$X_{disp} = R\cos(\theta_2) \tag{2.5.4}$$

$$Y_{disp} = R\sin(\theta_2) \tag{2.5.6}$$

where X_{mov} = movement of mark in x-direction, Y_{mov} = movement of mark in y-direction, X_{disp} = distance in x-direction from center of rotation to mark, and Y_{disp} = distance in y-direction from center of rotation to mark. Substituting (2.5.1), (2.5.2), and (2.5.3) into (2.5.4) and (2.5.5) yields

$$X_{disp} = \frac{Y_{mov}}{2\sin(\theta_1/2)} \tag{2.5.6}$$

$$Y_{disp} = \frac{X_{mov}}{2\sin(\theta_1/2)} \tag{2.5.7}$$

X_{disp} and Y_{disp} are obtained by measuring the movement of the marks on the wafer before and after rotating the wafer chuck a given amount. This is done prior to setting the mask in the mask holding plate and performing an alignment. This allows the operator to predict X_{mov} and Y_{mov} for different θ_1 inputs. Since the rotational inputs will be on the order of μrads, X_{mov} can be ignored. It can then be assumed that a rotational input will cause the marks to move only in the y-direction. The magnitude and direction that each mark will move is then simply a function of its distance from the center of rotation and the direction of the θ_1 input.

2.5.2 Magnification Error

Magnification error occurs when there is a scaling error between the alignment marks on the mask and the wafer. The cause of this error is the variability in the stretching of the CCL mask as it is pulled into contact with the wafer. The magnification error can be controlled by changing the gap between the mask and the wafer. Assuming the pitch of the marks on the mask is greater than on the wafer, the marks will skew inward if the gap is too large and will skew outward if the gap is too small. Figure 2.19 shows the experimentally determined magnification error for gaps ranging between 100 and 220 μm.

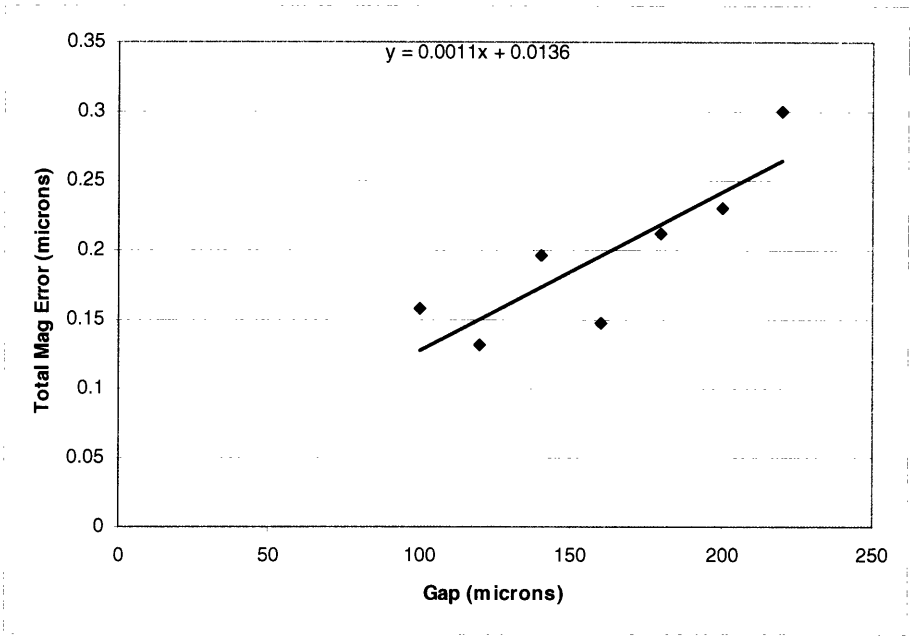

Figure 2.19: Magnification error for gaps ranging from 100 and 220 μm.

Figure 2.20 shows the strain of the mask versus the gap between the mask and wafer. Strains from previously run simulations at Draper Laboratory for gaps between 0 and 100 μm were determined, while strains determined experimentally were found for gaps between 100 and 220 μm. The experimental results compare somewhat favorably to the simulated results when differences between the two are considered: First, the simulation determined the strain for gaps up to 100 μm while the experimental strains were found for gaps between 100 and 220 μm. Secondly, temperature effects were not accounted for. Finally, the mask ring was fixed rigidly in place for the simulation when in reality this is highly unlikely to be the case.

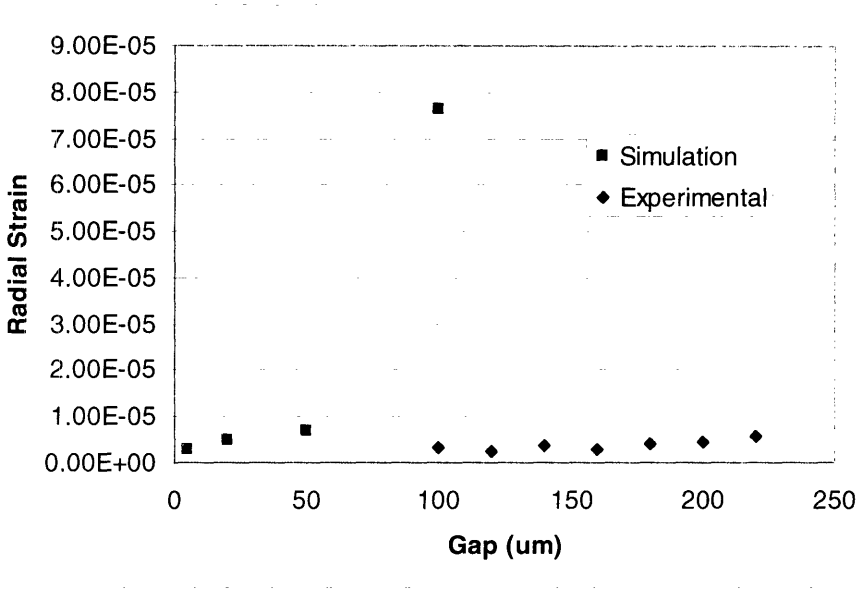

Figure 2.20: Strain versus gap. The strains were determined by a simulation for gaps ranging from 0-100 μm and were determined experimentally for gaps ranging from 100 μm-220 μm.

2.5.3 Image Fidelity

The size and resolution of the images captured with the dual microscopes are 640 by 480 pixels where 1 pixel is approximately 0.5 μm. The real alignment marks lacked the image fidelity of the simulated marks due to camera and pattern replication limitations. It is reasonable to expect alignment accuracies less than the simulated predictions due to these limitations. A set of closely aligned real marks is shown in Figure 2.21. It is obvious that the image quality of the real alignment marks is nowhere near that of the simulated marks. The dual microscopes also created "shading" or "shadowing" across the image which prevented the use of image enhancing techniques such as thresholding. The marginal image quality also inhibited the automated alignment system's ability to detect the location of the moiré fringes.

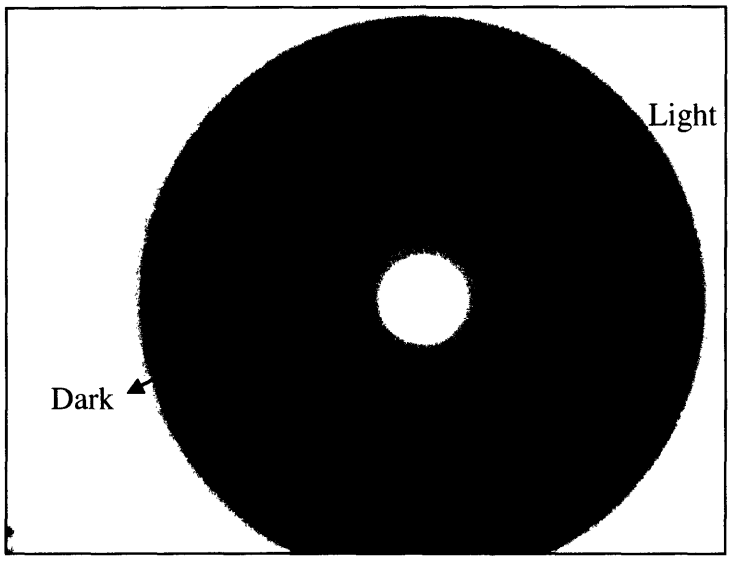

Figure 2.21: A set of closely aligned marks. There is noticeable shading/shadowing across the image.

The detractors of image fidelity (electronics noise, pattern replication, shadowing, vibrations, etc.) limit the ability of the imaging software to consistently determine locations on an image. This hinders the ability to locate both the centroid of the marks and the moiré fringe. In order to determine the effect of the noise, 50 consecutive images were taken of an alignment mark on the wafer (no moiré pattern). The centroid of the unmoved alignment mark was then analyzed. The results of this experiment are presented below in Table 2.5.

Table 2.5: Consistency of finding the center of a mark.

σ_X	0.21 pixels	0.10 μm
σ_Y	0.12 pixels	0.06 μm

Another experiment was conducted where 50 images consecutive images were captured of a closely aligned pair of marks (with a moiré pattern). The misalignment of the marks was determined for each image and the consistency of the misalignments were determined. The results of the experiment are presented in Table 2.6.

Table 2.6: Consistency of determining misalignment of a pair of marks.

σ_X	0.14 pixels	0.07 μm
σ_Y	0.20 pixels	0.10 μm

One would expect greater consistency in locating the centroid versus locating the centroid and then using that centroid to locate the moiré fringe. However, a comparison of the results in Table 2.5 and 2.6 shows that the standard deviations of the two experiments are nearly equal. This implies that vibrational and other image noise dominates the error in determining the misalignment. Based on this information, it was assumed that all alignment measurements had an error of ± ~0.1 μm.

2.5.4 Contact and Release Repeatability

Another hindrance to the alignment process is the relative movement between the mask and wafer that occurs when bringing the mask and wafer in and out of contact. The repeatability of the contact and release procedure was tested by performing 25 contact/release cycles and analyzing the alignment of a mark after each cycle. This experiment was performed a number of times with 3 test results listed in Table 2.7. Figure 2.22 shows the misalignment for the 25 contact/release cycles in relation to its one standard deviation radius. The results from test 1 indicate that after the first three contact/release cycles, the remaining 22 contact/release cycles demonstrated very good repeatability. This "settling" behavior seemed to be a common phenomenon when performing the repeatability tests. Possible causes of this behavior may include variable stretching of the mask as it is being pulled into contact and movement of the entire mask in the mask holding plate due to the force being exerted on it as it is brought into contact. Another source of error is the movement of the stages (*i.*e. "wiggle" of sliding stages) when the mask is brought into and out of contact with the wafer. Since each degree of freedom is controlled by a separate stage and each stage is stacked on top of each other, the errors from each are cumulative.

Table 2.7: Repeatability of contact and release.

Test	σ_X	σ_Y	σ_R
1	.062 μm	.055 μm	.083 μm
2	.100 μm	.101 μm	.142 μm
3	.124 μm	.061 μm	.138 μm

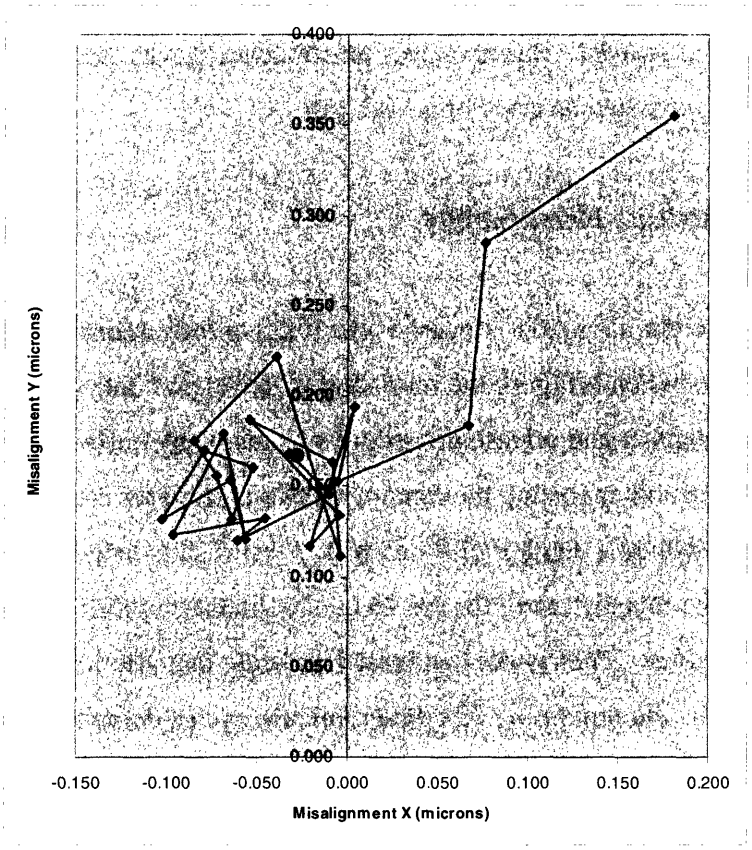

Figure 2.22: 25 contact/release cycles in relation to their standard deviation radius.

2.5.5 Commanded versus Actual Movement

A major obstacle to achieving an automated alignment system is the inconsistency of moving the mask with the piezo-actuated stages. Unlike the simulated alignment experiment, the commanded and actual movements of the wafer are not the same. Experiments were conducted to see if the movement of the wafer relative to what was

commanded by the piezo-actuators could be characterized. Experiments were performed for movements in the X and Y directions. The basic form of the experiment consisted of first closely aligning a set of marks, then incrementally moving the wafer in the positive direction to a certain commanded distance, moving it in the opposite direction until reaching the same commanded distance in the negative direction, then finally moving back to the starting position. Images were taken of the starting alignment and of the alignment after each commanded movement. These images were then analyzed to determine the actual wafer movements. The movement increments that were used were 0.5 μm, 1 μm, 2 μm, and 3 μm for the X and Y directions. The experiments showed that on average, the actual wafer movement was some fraction of the commanded amount. However, this fractional amount was wildly inconsistent. It appeared that there was a hysteresis effect present, but this could not be compensated for due to the inconsistency of the wafer movements. The likely cause of the inconsistent wafer movement is the rubber substrate gasket "gripping" the Pyrex ring of the CCL flex mask and therefore preventing the substrate from moving freely. Figure 2.23 shows a cross-sectional view of the mask and wafer chuck configuration. The area where the gasket contacts and "grips" the glass ring is noted.

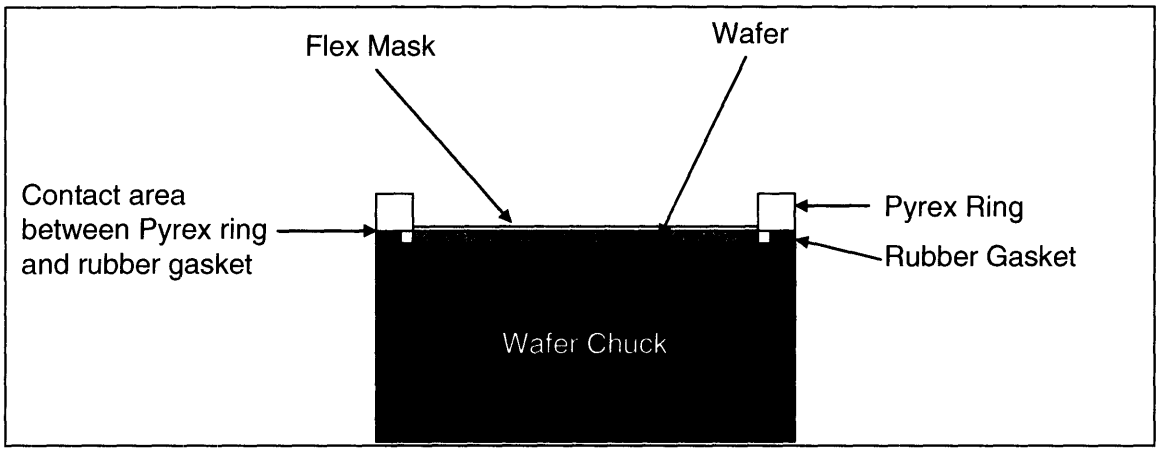

Figure 2.23: Cross-sectional view of the mask and wafer chuck configuration.

The rubber gasket "gripping" theory is supported by the fact that the actual substrate movements were closer to the commanded movements when the gap was increased. Figure 2.24 shows an example of the observed hysteresis effect for movement increments

of 1 μm in the x-direction. Table 2.8 compares the average of commanded movements of 1 μm in the positive and negative x-direction at gaps of 100 μm and 130 μm.

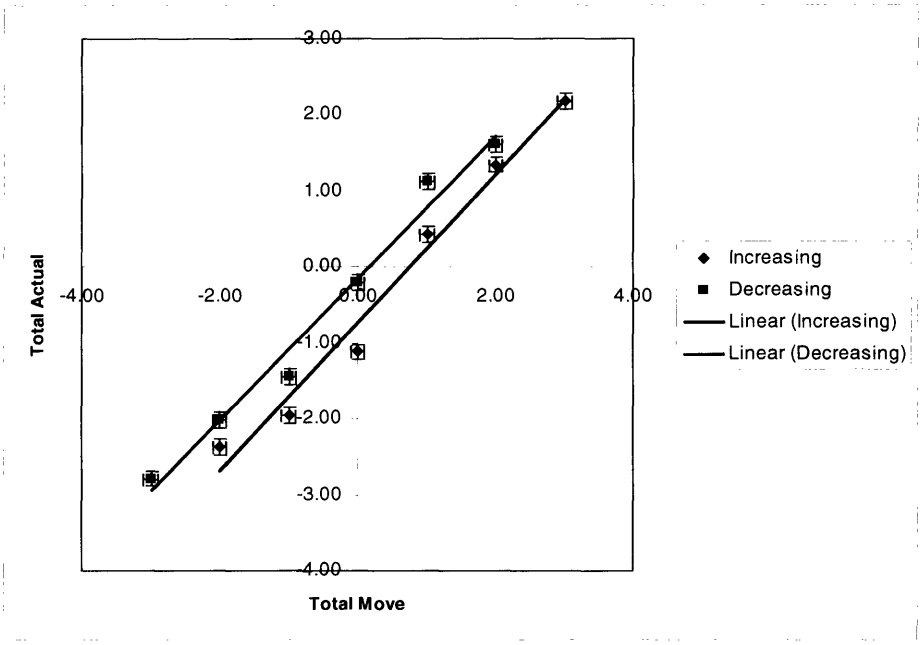

Figure 2.24: Hysteresis effect of substrate movements.

Table 2.8: Average of 1 μm commanded movements in the x-direction for gaps of 100 μm and 130 μm.

	Average Movement Gap = 100 μm	**Average Movement Gap = 130 μm**
+ Direction	0.642	0.828
- Direction	-0.828	-0.907

2.5.6 Consequences of Alignment Issues

The obvious consequence of the experimental alignment issues is the reduction of the alignment accuracy that was predicted in the alignment simulation. At a minimum, one could expect an alignment measurement uncertainty of ± ~0.1 μm due to image noise. However, pattern placement over the area of a wafer is expected to be diminished due to

rotation and magnification errors. It is therefore fair to assume that the most accurate pattern placements will occur near the alignment marks.

Another consequence of the experimental alignment issues is the decreased accuracy of the automated alignment system. Cumulative error effects from each of the issues will certainly degrade the capability of the system.

2.6 Alignment Experiment and Results

An alignment experiment was conducted to determine the alignment accuracy of the current CCL/moiré alignment system at Draper Laboratory. For the experiment, Cr was patterned on the wafer and flex mask. Resist was then spun on the wafer. After alignment was achieved, the resist was exposed and developed. Pattern placement errors were determined by moiré alignment marks at various locations on the wafer. The automated alignment system was not employed for this experiment since the various issues described in the previous section (mainly contact/release repeatability and commanded versus actual movement) made it less accurate than manual alignment. Table 2.9 presents the raw pattern placement error. X_{abs} and Y_{abs} are the absolute values of the pattern placement error in the x- and y- directions. Figure 2.25 is a plot of the recorded pattern placement error for each of the alignment marks on the wafer.

Table 2.9: Pattern placement error for raw data (μm).

	Ave.	σ	Min.	Max.
X	-0.0337	0.257	-0.476	0.589
Y	0.186	0.393	-0.391	1.062
R	0.384	0.316	0.111	1.214
$\mathbf{X_{abs}}$	0.197	0.161	0.037	0.589
$\mathbf{Y_{abs}}$	0.306	0.302	0.029	1.062

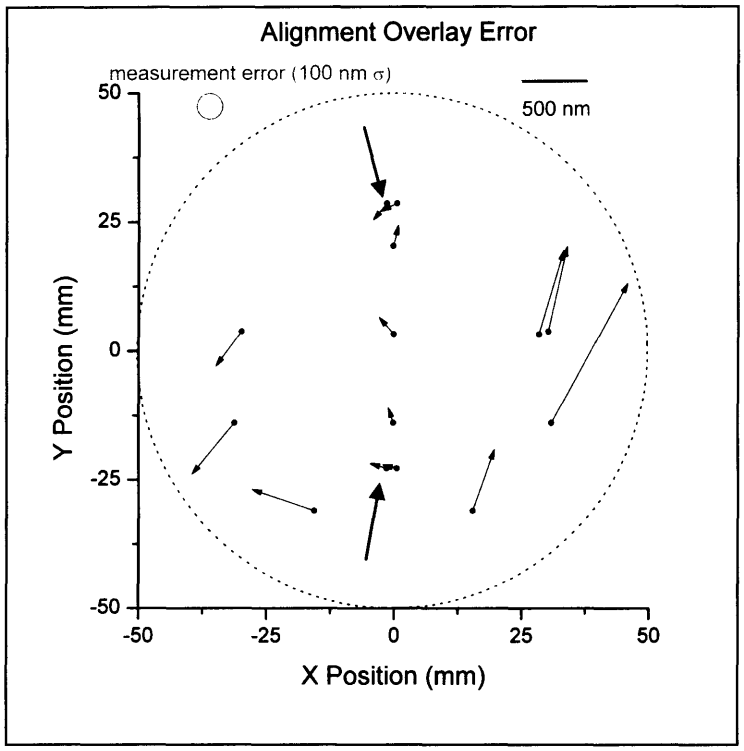

Figure 2.25: Pattern placement error for various locations on the wafer. The locations of the marks used for the alignment are highlighted.

It is noticeable in Figure 2.25 that the pattern placement is much better along the line between the alignment marks. Table 2.10 presents the pattern placement error data along the "alignment mark line."

Table 2.10: Pattern placement error data along "alignment mark line" (μm).

	Ave.	σ	Min.	Max.
X	-0.082	0.060	-0.127	0.037
Y	0.040	0.104	-0.127	0.159
R	0.143	0.024	0.111	0.171
$\mathbf{X_{abs}}$	0.093	0.039	0.037	0.127
$\mathbf{Y_{abs}}$	0.093	0.051	0.029	0.159

The pattern placement accuracy along the "alignment mark line" compared to other locations on the wafer is a bit surprising since in theory, errors stemming from x, y, θ, and magnification should be fairly consistent across the wafer. For example, if the marks on the "alignment mark line" are excluded, it would appear that there is a large rotational error. However, the marks on the "alignment mark line" do not imply this. It is possible that the inconsistent pattern placement accuracies on the wafer are the result of non-radially symmetric stretching of the mask. This could be caused by a number of reasons to include variations in thermal expansion or the manner in which the mask is clamped down. Additional experiments using the same mask may reveal the cause of this behavior.

2.7 System Improvement

The automated alignment system presented in this chapter will only be possible and/or accurate if a number of problematic issues are addressed. First, the image quality is currently marginal. Microscope improvements (eliminate "shading") would greatly improve the ability of the user to align the marks and of the image analysis software in detecting the moiré fringe location. Second, image noise is currently the dominant factor that contributes to the misalignment measurement error. Better vibration dampening and/or microscope improvements would likely decrease image noise. Third, the contact and release repeatability is sub-par and is a main contributor to the inaccuracy of the automated alignment system. Further experiments could track down the cause of this problem, but places to start include holding the mask more rigidly by way of vacuum or some other method and/or replacing the current stack of Z, X, Y, and θ stages with a single flexure stage. Lastly, the inconsistent wafer movements make manual alignments difficult and an automated alignment impossible. Eliminating the rubber gasket on the wafer chuck would increase the consistency of the wafer movements. Without the gasket, the mask and wafer could be brought into intimate contact by applying pressure to the top side of the mask instead of pulling the mask into the wafer by vacuum.

Nevertheless, the current CCL with moiré-based alignment system demonstrated mean, absolute pattern placement errors of ~200 nm and ~300 nm in the x- and y-directions respectively, which is an improvement over a typical conventional contact lithography procedure conducted at the Draper MEMS fab.

Chapter 3

Cr/AlN/Mo Stack Etch Using Chlorine Reactive Ion Etching (RIE)

In the previous resonator fabrication process, the wet etch of the AlN produced a sloped sidewall. This sidewall angle imposes limitations on feature sizes. A straight sidewall via Cl-based dry etching will allow the reduction of feature sizes and make the inclusion of notched resonator-tether interfaces possible. This section provides a literature review of Cr, AlN, and Mo etching, discusses Cl-based dry etching experiments, and presents results from the experiments.

3.1 Review of Chromium Etching

Chromium is known to etch at considerable rates in standard Cr wet etchants and chlorine based dry-etch chemistries. Since a wet etch of Cr is isotropic and therefore undesirable to the fabrication process, only dry etch chemistries were investigated. The gas mixtures that are known to etch Cr are Cl_2 or Cl-based gas, $Cl_2 + O_2$, and $Cl_2 + O_2 + Ar$ (or another noble gas) [17]. The etch product that is produced using Cl-based chemistries is CrO_2Cl_2 and results from the following chemical reaction proposed in [18]

$$Cr + 2O^* + 2Cl \rightarrow CrO_2Cl_2 \qquad (3.1.1)$$

where O* is reactive oxygen. The advantages of using a Cl-based chemistry include high reactivity and a low etch product (CrO_2Cl_2) boiling point of about 117°C at one atmosphere, which makes it volatile in gas plasmas [18]. In [18], the etch rate of Cr seemed to be most dependent on the presence of Cl and O_2 since additions of gases such as Ar and N_2 had no considerable effect on etch characteristics. Furthermore, in both

[17] and [18] it was noted that increasing the O_2 concentration increases the Cr etch rate. It is also noted in [18] that the etch increases until the O_2 concentration reaches a saturation limit of ~50%.

3.2 Review of Aluminum Nitride Etching (AlN)

3.2.1 Wet Etching of Aluminum Nitride

An assortment of solutions has been shown to etch AlN with varying degrees of effectiveness. As stated in Chapter 1, AZ400K, a common photoresist developer, was originally used to etch the AlN in the fabrication of the Draper MEMS resonator. In the previous process, AZ400K was selected because of its previously demonstrated effectiveness. In [19], AlN layers up to 1 μm thick were shown to etch with perfect selectivity over GaN and Al_2O_3 and without any dependence on crystallographic orientation. The etching also showed reaction-limited behavior by having strong dependencies on etchant concentration, crystalline quality, temperature, and a typical reaction-limited etch activation energy (~15.5 kcal mol^{-1}) [20]. In addition, AlN etching in AZ400K proved to be completely selective over the Ni (original top metal), NiV and Cr, Mo, and SiO_2 layers of the resonator and was self-limiting, making AZ400K a logical choice for etching of the AlN.

However, the self-limiting etch produces a sloped sidewall as mentioned in Chapter 1. Based on previous publications, it seems likely that the sloped sidewall results from etching along the $(1\bar{1}01)$ planes of the AlN. AlN has a polar wurtzite structure as shown in Figure 3.1. This structure is essentially a hexagonal closed-packed stacking of the "B" type atoms (N^{3-}) with the "A" type atoms (Al^{3+}) in the tetragonal interstitial positions [21]. This configuration causes a polarity in the direction of the c-axis due to basal planes of different polarities.

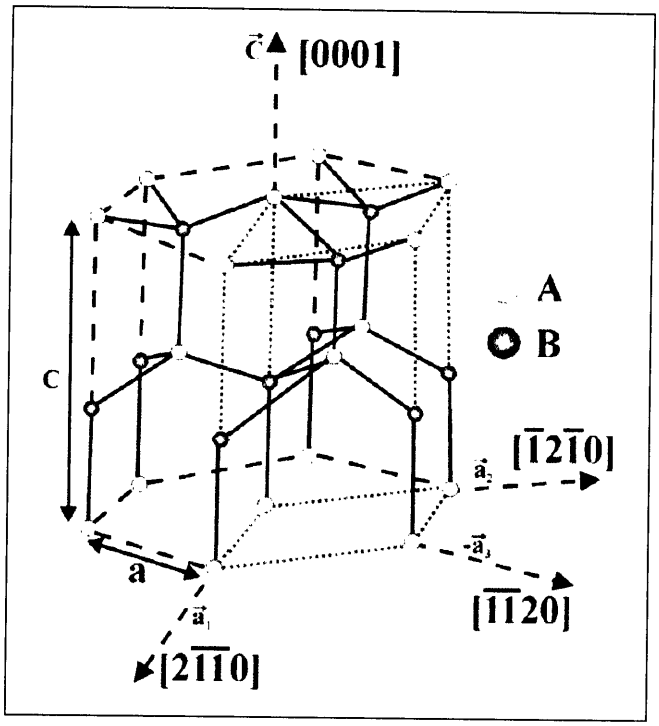

Figure 3.1: Polar wurtzite crystal structure [21].

In [22], it was determined that the nitrogen polarity (0001) basal plane etched rapidly in a KOH solution, while the aluminum polarity basal plane and prismatic $(1\bar{1}01)$planes were not etched. The sidewall angle of the AlN etched in AZ400K as shown in Figure 3.2 was measured to be $61.2^{\circ} \pm 7^{\circ}$. This range of error for the measurement is limited by the pixelation of the SEM images. However, the measurement appears to be consistent with 66.6°, the angle between the (0001) and $(1\bar{1}01)$ planes.

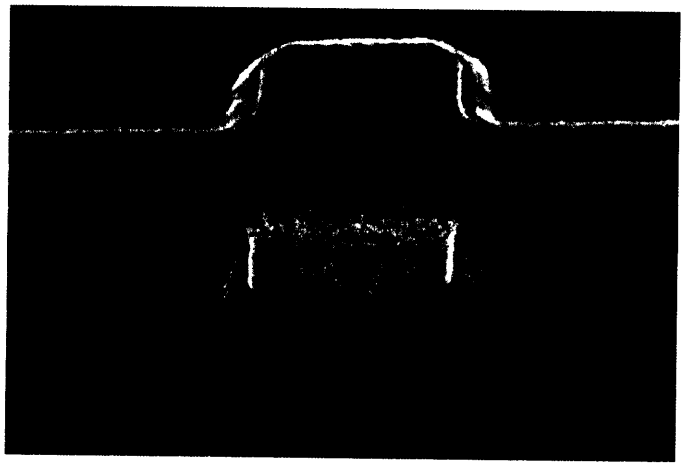

Figure 3.2: Etched device with sloped sidewalls.[1]

According to [23], the $(1\bar{1}01)$ planes are energetically stable because they cut through a small number of bonds. Therefore, it is believed the AlN was etched along those planes. Also, supporting this assertion is the fact that hexagonal hillocks, similar to the conical structures that were observed in the AZ400K etch (see Figure 3.3) were also reported in [22].

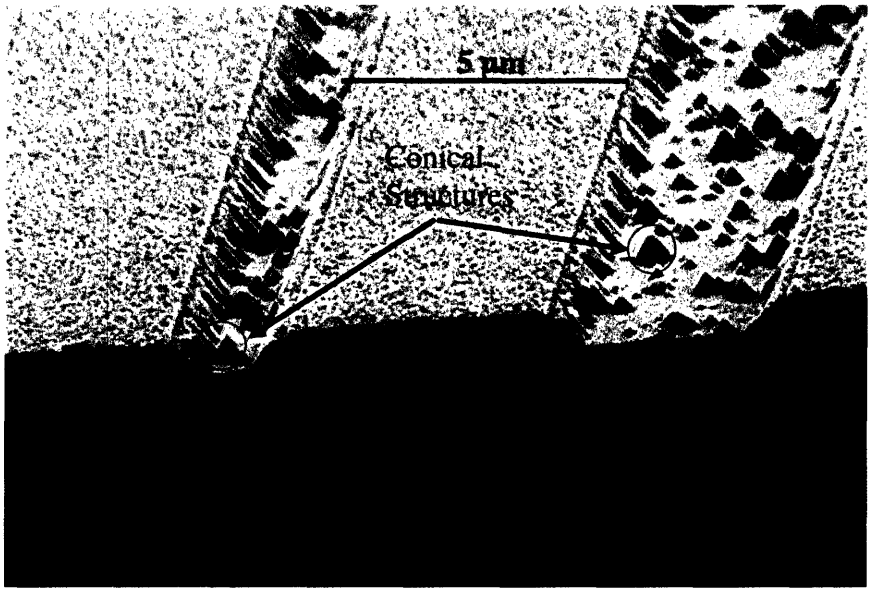

Figure 3.3: Conical structures present when AlN etched with AZ 400K.

3.2.2 Dry Etching of Aluminum Nitride

Aluminum nitride has been shown to etch in various Cl-based plasma chemistries. Conventional reactive ion etching with capacitively-coupled parallel plate configurations have shown limited etch rates even at high ion energies due to the high bond energy of AlN. The highest etch rates have been achieved in high-density plasma reactors such as electron cyclotron resonance (ECR) microwave plasma sources and inductively coupled plasma (ICP) sources. The high-density plasma sources allow the ion density to be decoupled from the bias that is applied to the substrate. This allows high ion densities and low biases which result in substantial etch rates, but with greater selectivity and less damage [24]. Etch rates exceeding 2000Å/min have been achieved with high density

plasma sources using Cl-based chemistries at process pressures between 1 and 2 mTorr and at DC Biases between 150 and 200 V [25, 26].

The etch product using Cl-based chemistries is $AlCl_3$ [25]. Some gas mixtures that have shown to etch AlN at a significant rate include Cl_2/Ar, Cl_2/H_2, BCl_3/Cl_2/Ar, and $Cl_2/CH_4/H_2$/Ar [27-30]. The addition of Ar to the Cl chemistry enhances the ion bombardment and therefore increases bond breaking, which precedes the etch product formation [28]. The addition of H_2 removes nitrogen as NH_3 and therefore increases the etch product desorption [30]. The addition of BCl_3 to the gas mixture works similarly to Ar in that it increases the sputter desorption of the etch products due to the heavier BCl_x ions [25]. The addition of CH_4 is believed to increase the etch rate due to the formation of highly volatile $AlCl_3$ or by some other etch mechanism which is enhanced by CH_4 [29]. Regardless of the plasma chemistry, the degree of anisotropy and degree of damage seems to be determined by the balance between the physical and chemical etch mechanisms.

3.3 Review of Molybdenum (Mo) Etching

Molybdenum is known to etch at considerable rates in F-based and Cl-based gases [31]. Typically both types of gas mixtures include O_2 since it has been shown to improve etch rates. Fluorine- and oxygen-based mixtures are believed to produce etch products such as $MoOF_4$ [32]. Chlorine and oxygen mixtures are believed to form molybdenum oxychlorine (MoO_xCl_y) [31]. In both [31] and [33], increases in ion bombardment did not always increase the etch rate, which would indicate the importance of the chemical etching.

3.4 Chlorine RIE Experiments

The challenge of the chlorine RIE experiments was to find etch processes for each material in the stack that were compatible with the entire stack etch, such that the etch process didn't undercut the layer being etched or the layer(s) above it. A process with selectivity to the layer below it would be considered ideal.

3.4.1 Equipment and Materials

All RIE processes were performed using the Nexx System Cirrus 150 ECR plasma etch system at the Harvard University Center for Nanoscale Systems (CNS). The process pressure was held constant at 2.0 mTorr and the He backside-cooled wafer chuck was held at 20°C for all etch processes. The etched samples were cleaved wafer pieces that were placed in the load-lock chamber on a quartz wafer that was bonded to a silicon wafer. The goal of the experiments was to obtain an etch characterization (etch rate, etch quality, sidewall profile) for the "stack" (SiO_2, "seed" AlN, Mo, AlN, and Cr) using a plasma-enhanced chemical vapor deposition (PECVD) SiO_2 etch mask.

The PECVD oxide etch mask was patterned on the stack in an array of lines with width ranging between 2 μm and 4 μm at center-to-center spacing from 2 μm to 8 μm. This SiO_2 etch mask was patterned by dry etching in fluorine-based plasma in a Surface Technology Systems RIE (see Appendix C) or wet etched with buffered hydrofluoric acid (BHF). Shipley 1813 resist served as the etch mask for the PECVD oxide.

Etch rate characterizations were gathered for each material component of the "stack" using the oxide mask and for a blanket film of PECVD SiO_2 which was used to estimate the etch rate of the mask. Etch rates for materials with the patterned oxide mask were determined by cross-sectional scanning electron microscopy (SEM), while rates for the blanket SiO_2 were determined by ellipsometer measurements. Table 3.1 lists the different samples, their material thicknesses, and SiO_2 etch mask thickness (if applicable).

Table 3.1: Etched materials, thicknesses, SiO_2 etch mask thickness.

Sample	Material(s) Thickness (Å)	SiO_2 Mask Thickness (Å)
"stack" (Mo, AlN, Cr)	1500, 5000, 1500	4000
Cr	1500	2000
AlN	5000	4000
Mo	1500	4000
SiO_2	4000	none

3.4.2 Experimental Process

Based on previous literature [26, 28-30] on the etching of the stack materials, the initial gas chemistries that were tested were Cl_2/H_2, Cl_2/Ar, and Cl_2/O_2. Table 3.2 lists some AlN etch recipes found in these references that were used as general reference points in developing a recipe for the "stack" etch process. Table 3.3 lists the starting recipes that were tested and their respective target etch material.

The initial etch recipes were kept as consistent with the literature as possible. Process pressure was set low as low as possible (2 mTorr) and microwave source power was set as high as possible (500 W). The DC bias was set by adjusting the RF power until a comparable voltage to the literature was achieved. The flow rates that were used for the experiments differed from that in the literature due to equipment differences. However, the gas ratios were comparable.

Table 3.2: AlN etch recipes taken from literature.

Recipe	Cl_2 (sccm)	H_2 (sccm)	Ar (sccm)	O_2 (sccm)	Pressure (mTorr)	Microwave/ Source Power (W)	RF Power (W)/ DC Bias (V)
Cl_2/H_2 [7]	15	10	0	0	2	500	250/-250
Cl_2/H_2 [9]	10	15	0	0	1	1000	Not listed/-150
Cl_2/Ar [7]	20	0	5	0	2	500	250/-150
Cl_2/Ar [10]	5	0	10	0	1.5	1000	450/-160

Table 3.3: Initial etch recipes.

Recipe	Target Materials	Cl_2 (sccm)	H_2 (sccm)	Ar (sccm)	O_2 (sccm)	Pressure (mTorr)	Microwave Power (W)	RF Power (W)/ DC Bias (V)
Cl_2/H_2	AlN, Cr, Mo	6	4	0	0	2	500	200/-250
Cl_2/Ar	AlN, Cr, Mo	6	0	1.5	0	2	500	200/-250
Cl_2/O_2	Cr, Mo	7.5	0	0	1.5	2	500	200/-250

For this first set of experiments, the patterned materials also had Shipley 1813 photoresist on top of the SiO_2 serving as an additional mask layer. After the materials were etched in the different chemistries, SEMs determined that the resist layer needed to be eliminated because it tended to melt and flow, which ruins the pattern fidelity (see Figure 3.4). It was also determined that the Cl_2/Ar chemistry at the current DC bias level caused an unacceptable amount of damage and eroded the SiO_2 mask layer at too great of a rate (~750 Å/min). No other definitive data could be gathered due to the melting of the resist.

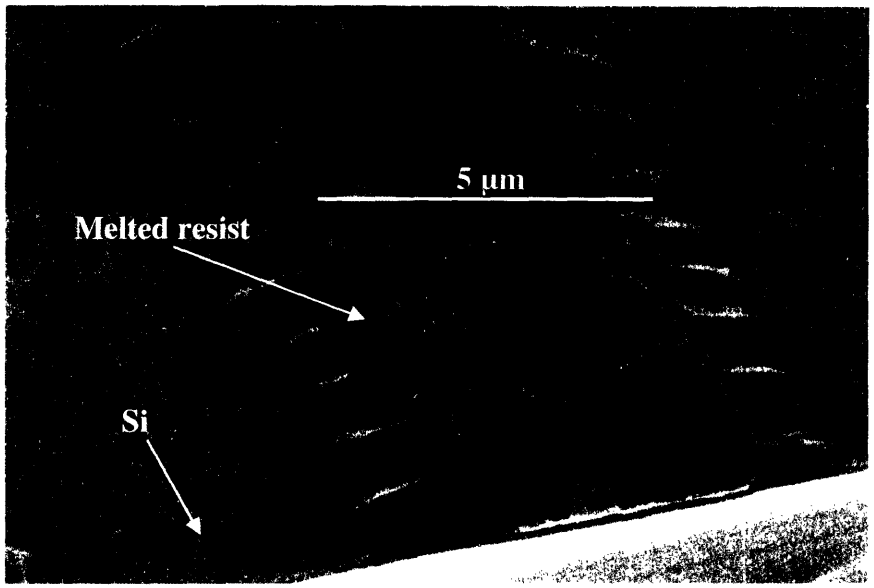

Figure 3.4: Melting and flowing of photoresist.

Table 3.4 lists the etch recipes that were tested for the second set of experiments. For this set, etches were performed with the Cl_2/H_2 and Cl_2/O_2 mixtures at RF power settings of 200 W (HI) and 110 W (LO), the second of which corresponds to a DC bias of -150 V ± 10 V. The Cl_2/Ar chemistry was only used at the LO setting since it was already determined that this chemistry was undesirable at the HI setting. A gas chemistry of pure Cl_2 at a flow rate of 7.5 sccm was also used at the LO setting. Table 3.5 shows the etch rates of the materials for the different etch recipes. It is important to note that the AlN and Mo etch rates at this point were crude estimates due to the small number of etches performed on those materials up to that point in time.

Table 3.4: Etch recipes for second set of experiments.

Recipe	Cl_2 (sccm)	H_2 (sccm)	Ar (sccm)	O_2 (sccm)	Pressure (mTorr)	Microwave Power (W)	RF Power (W)/ DC Bias (V)
Cl_2/O_2 LO	7.5	0	0	1.5	2	500	110/-150
Cl_2/O_2 HI	7.5	0	0	1.5	2	500	200/-250
Cl_2/H_2 LO	6	4	0	0	2	500	110/-150
Cl_2/H_2 HI	6	4	0	0	2	500	200/-250
Cl_2/Ar LO	6	0	1.5	0	2	500	110/-150
Cl_2 LO	7	0	0	0	2	500	110/-150

Table 3.5: Etch rates for second set of experiments (Å/min).

Recipe	SiO_2	Cr	AlN	Mo
Cl_2/O_2 LO	~40-100	~600	~0	Rate not determined
Cl_2/O_2 HI	~200	~750	~0	Rate not determined
Cl_2/H_2 LO	~200	~0	~200	~375-500
Cl_2/H_2 HI	~400	~100	~666	~500
Cl_2/Ar LO	~200	~150	~1000	~1500
Cl_2 LO	~400	~400	~700	~1500

After the second set of experiments it was determined that none of the recipes exhibited adequate selectivity for the entire "stack" of materials over the SiO_2 mask (see Table 3.5) and therefore none seemed suitable to etch all three layers of the stack.

However, the Cl_2/O_2 LO recipe was selected to etch the Cr layer since it etched anisotropically, showed high selectivity over the SiO_2, and its inability to etch the AlN at an appreciable rate provided a good etch "stop". Figure 3.5 shows a slight overetch (~10%) of the Cr and how it "stops" on the AlN. Figure 3.6 shows etch depth versus etch time for Cr with the Cl_2/O_2 Lo recipe. A linear fit to the data gives an etch rate of ~675 Å/min.

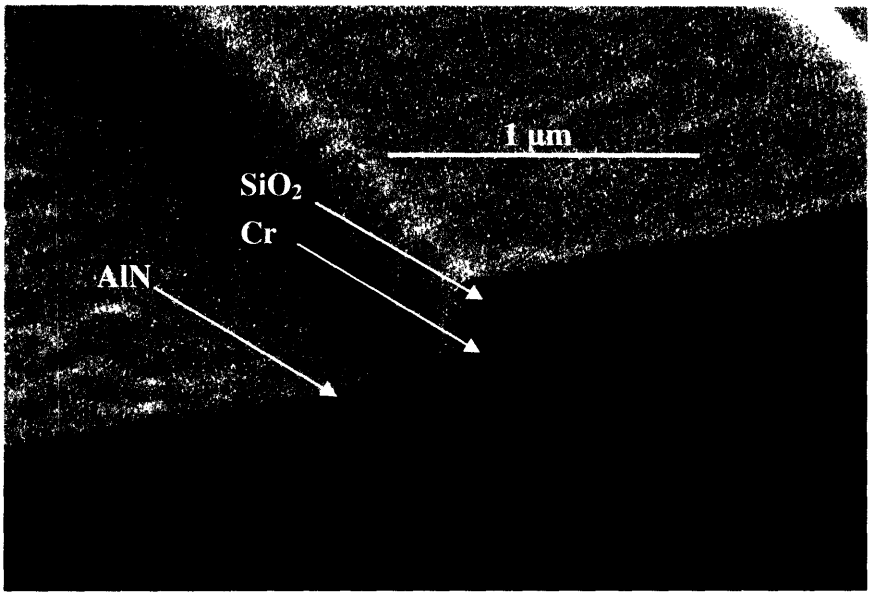

Figure 3.5: 2 minute 30 second etch of Cr with Cl_2/O_2 LO recipe. This 10% overetch stops on the AlN.

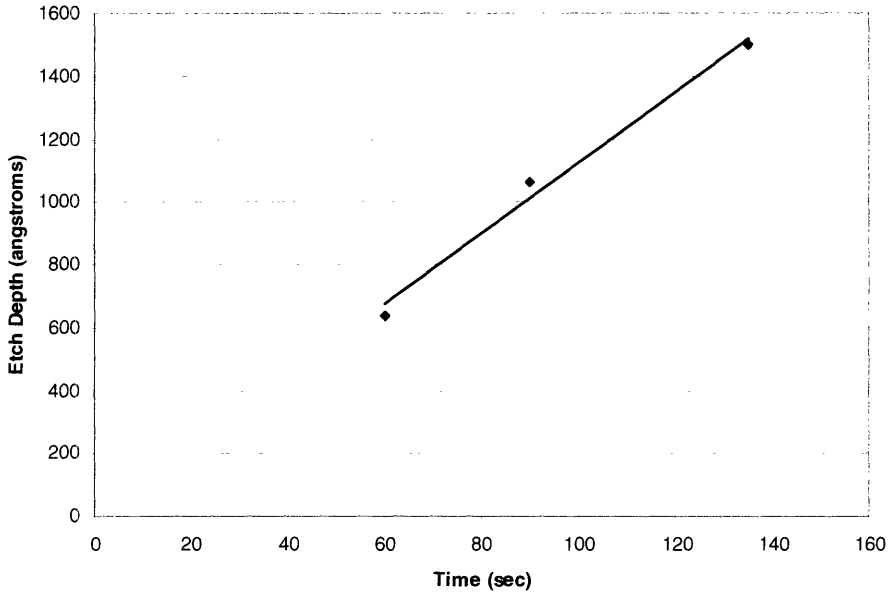

Figure 3.6: Etch depth vs. etch time of Cr with Cl_2/O_2 recipe. Linear fit gives an etch rate of ~675 Å/min.

A third set of experiments aimed to narrow down the choices for the etching of the AlN and Mo since accurate etch rates had not been gathered for these materials up to that

point. The recipes were selected in an effort to avoid etching the Cr if the SiO_2 mask was eroded, and therefore all had low Cr etch rates. The etch process times and increments for this set of experiments and successive sets were based on the previous sets' data and visual cues. Table 3.6 shows the etch rates that were observed for the third set of experiments. The results were fairly consistent with the second set except for the etch rates of the AlN with the Cl_2/Ar LO and Cl_2 LO recipes. A much quicker etch rate (an increase of ~600 Å/min (60% for Cl_2/Ar LO and 85% for Cl_2 LO)) was observed for these two chemistries.

Table 3.6: Etch rates for third set of experiments (Å/min).

Recipe	SiO_2	AlN	Mo
Cl_2/H_2 LO	~200	~200	~500
Cl_2/H_2 HI	~450	~755	~500
Cl_2/Ar LO	~275	~1666	~1500
Cl_2 LO	~350	~1250	~1500

After this set of experiments the recipes to etch the AlN and Mo were narrowed down to Cl_2/Ar LO and Cl_2 LO since they exhibited the best selectivity to the SiO_2 mask. The Cl_2/Ar Lo recipe appeared to have a slightly better sidewall angle than the Cl_2 LO recipe, but the sidewalls did not appear to be as smooth. It was also observed that both recipes undercut the Mo, with the undercut from the Cl_2 LO recipe being very severe. Figure 3.7 and 3.8 show the undercut effects of a ~2.5 minute overetch (250%) of the Mo for the Cl_2/Ar LO and Cl_2 Lo recipes.

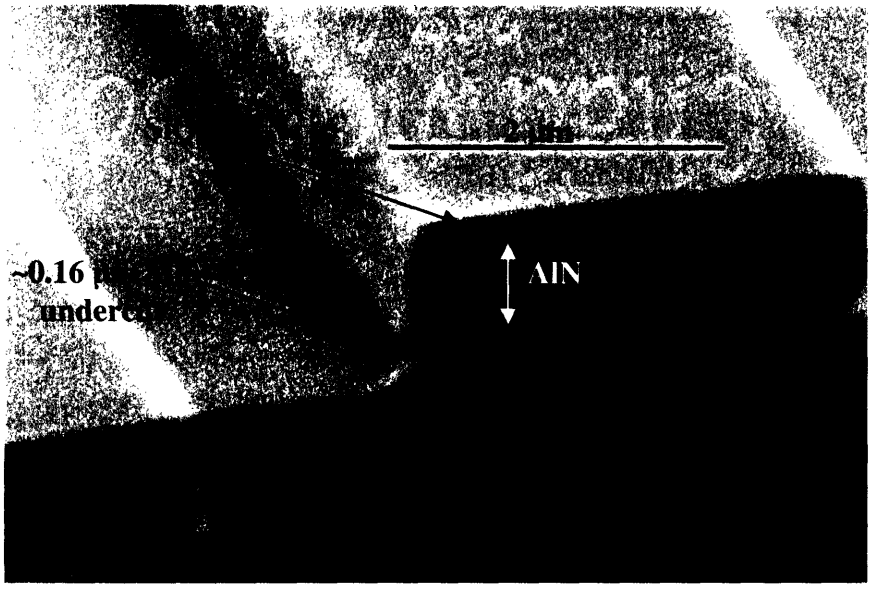

Figure 3.7: Undercut effects of ~2.5 minute overetch (250%) of Mo with Cl_2/Ar LO recipe.

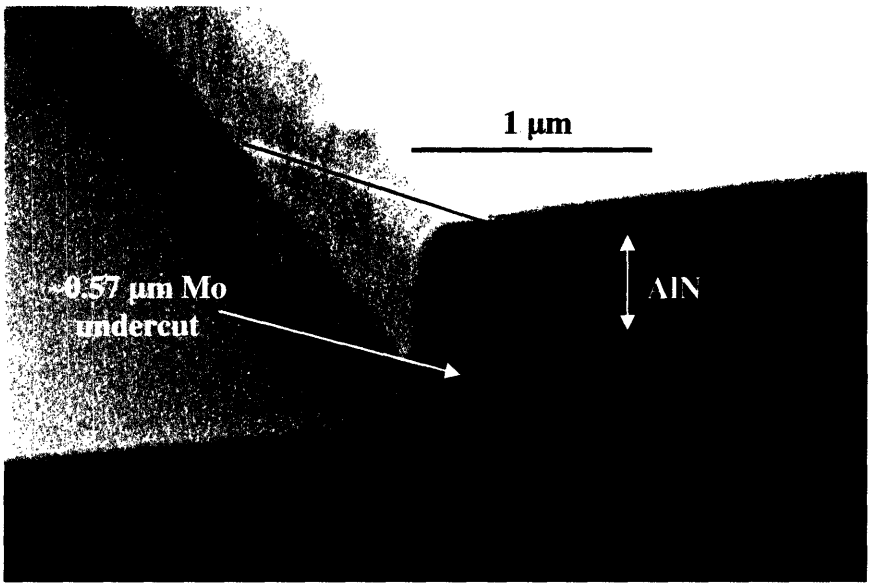

Figure 3.8: Undercut effects of ~2.5 minute overetch (250%) of Mo with Cl_2 LO recipe.

The fourth set of experiments aimed to get better etch rate characterizations of the AlN and Mo for the Cl_2/Ar LO and Cl_2 LO recipes. Table 3.7 presents the etch rates for the materials in the two etch recipes. The etch rates for this set of experiments were quicker than what was observed in the previous sets. The greatest etch rate increase was ~500 Å/min which was recorded for Mo using Cl_2/Ar LO (33% increase) and AlN using Cl_2

LO (40% increase). Figures 3.9 and 3.10 presents plots of etch depth versus time for the AlN etch in Cl_2/Ar LO (~1700 Å/min) and Cl_2 LO (1750 Å/min) recipes respectively.

Table 3.7: Etch rates for fourth set of experiments (Å/min).

Recipe	SiO_2	AlN	Mo
Cl_2/Ar LO	~360	~1700	~2000
Cl_2 LO	~350	~1750	~1800

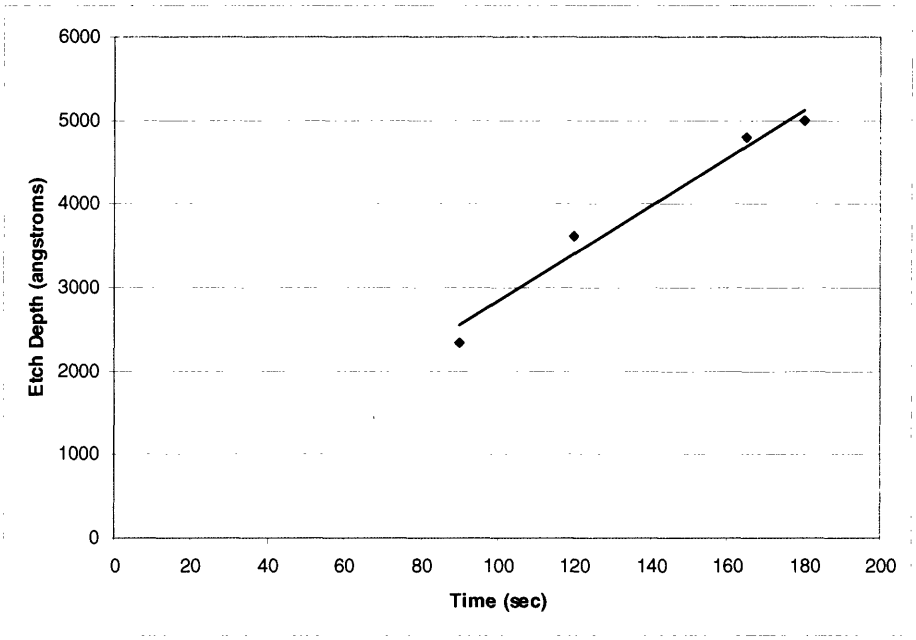

Figure 3.9: Etch rate of AlN with Cl_2/Ar LO recipe (~1700 Å/min).

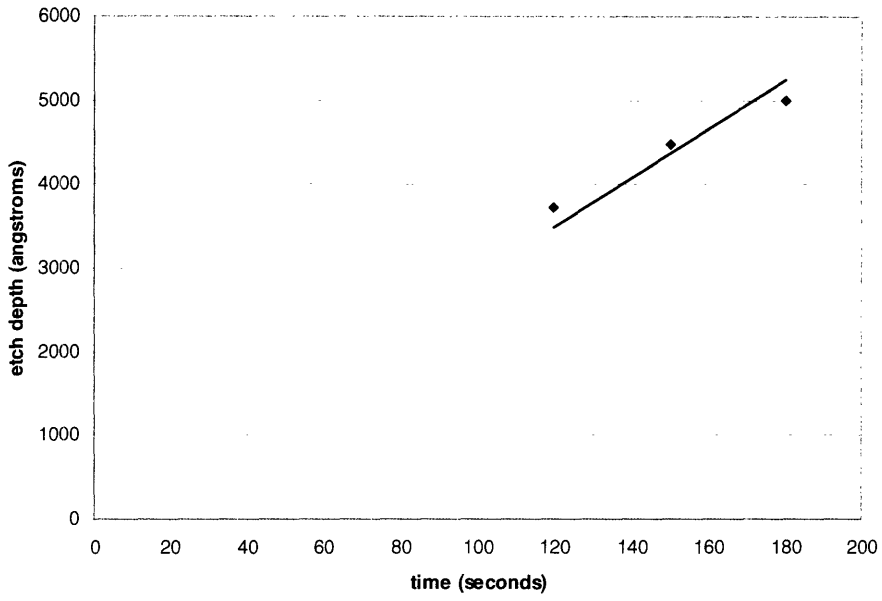

Figure 3.10: Etch rate of AlN with Cl_2 LO recipe (1750 Å/min).

The etch rate inconsistency seemed likely to be the result of some unknown change in chamber conditions, likely due to differences in previous users' etch recipes. Supporting this theory is the fact that a monthly chamber clean performed by Harvard CNS personnel between the fourth and fifth set of experiments coincided with etch rate reductions (~25%). The etch rate's inconsistency and dependency on chamber conditions reinforced the need to etch a "stack" sample prior to etching actual devices.

Based on the similar etch rates of the AlN with the two etch recipes, the Cl_2/Ar LO recipe was selected to etch the AlN since it produced the better sidewall angle. Figures 3.11 and 3.12 show etches of AlN with the Cl_2/Ar LO and Cl_2 LO recipes respectively. The sidewall angles for the Cl_2/Ar LO recipe were ~80° while the sidewall angles for the Cl_2 LO recipe were ~75°.

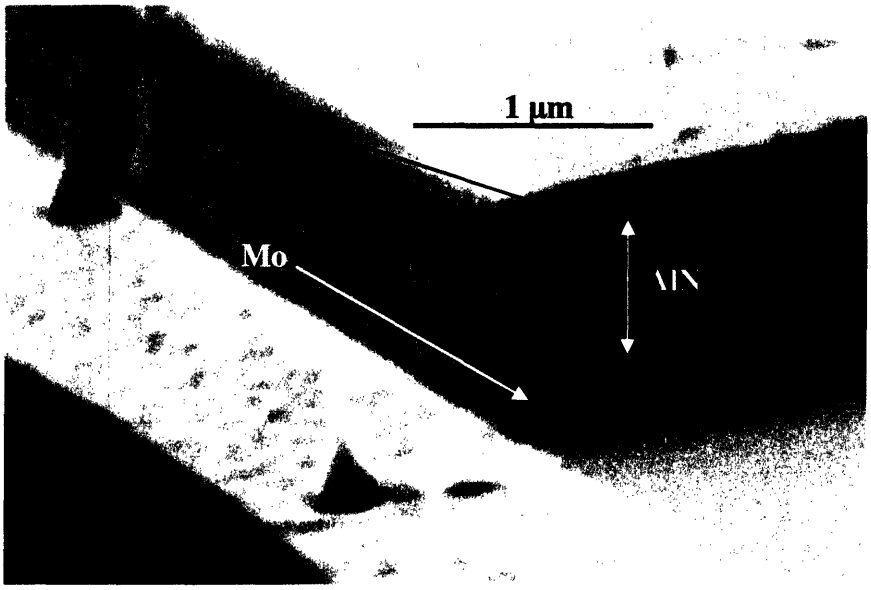

Figure 3.11: AlN etch with Cl_2/Ar LO recipe.

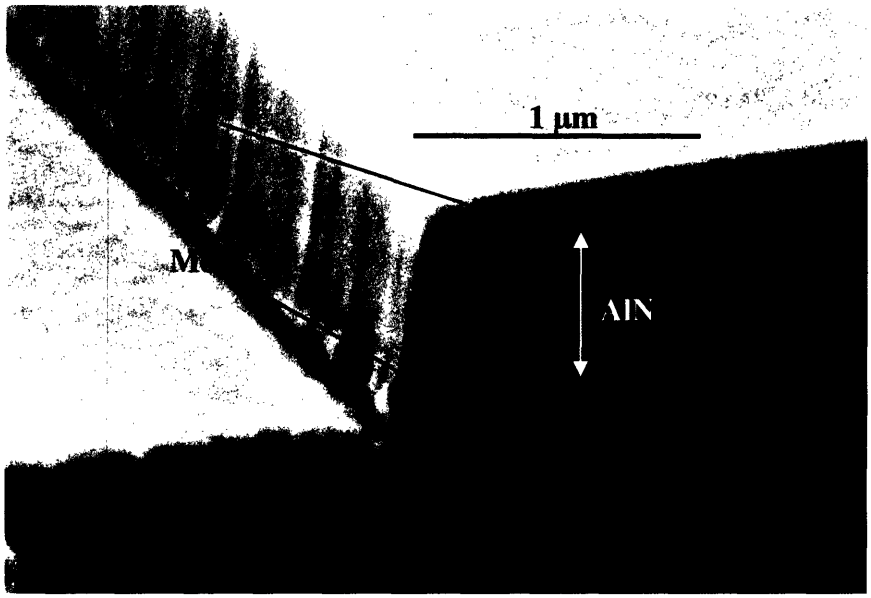

Figure 3.12: AlN etch with Cl_2 LO.

A fifth set of experiments was set up to determine an alternative etch chemistry that could etch the Mo with little or no undercut. A CF_4/O_2 etch recipe was tested to see if it would provide better results. The etch parameters for this recipe were the same as the Cl_2/Ar LO recipe except that the gas flows were CF_4 = 6 sccm and O_2 = 1.5 sccm. This etch

chemistry was selected based on [33] and the fact that the original fabrication process used a similar plasma chemistry and observed no Mo undercut.

In order to test the CF_4/O_2 recipe, the Cr and AlN were etched away with the Cl_2/O_2 LO and Cl_2/Ar LO recipes respectively. The CF_4/O_2 recipe etched the Mo with no observable undercut (see Figure 3.13) and therefore was selected as the gas chemistry to etch the Mo layer.

In addition to the CF_4/O_2 recipe, two alternate Cl_2/Ar recipes were tested in order to see if the etch rate of the AlN could be reduced while keeping the same anisotropy. The high etch rate that was observed in the fourth set of experiments made it difficult to stop at the Mo layer and also ran the risk of quickly etching through the Mo layer and subsequently undercutting it. Therefore, a slower, more controllable etch rate was desirable. One etch recipe had a lower microwave power setting of 300 W while the other recipe reduced the RF power to 75 W (DC bias = -110V). Neither of the alternate Cl_2/Ar test recipes proved to be more advantageous than the Cl_2/Ar LO recipe. Both test recipes slowed the AlN etch rate down, but did not slow the SiO_2 etch rate making them undesirable options.

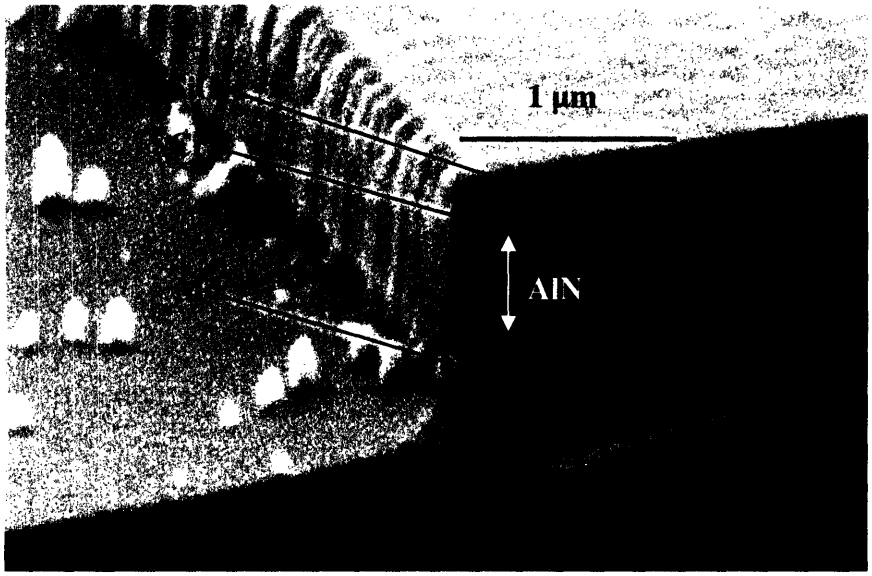

Figure 3.13: CF_4/O_2 overetch (25%) of Mo showing no observable undercut.

3.4.3 Stack Etch Results

The final gas chemistries and parameters are listed in Table 3.8 and the approximate material etch rates for the designated chemistries are listed in Table 3.9. Figures 3.14-3.19 show a sequence of etches through the stack of materials. It does not appear that the Cl_2/Ar LO recipe undercuts the Cr and the CF_4/O_2 does not appear to undercut the Cr or AlN.

Table 3.8: Final etch chemistries and parameters.

Layer to be etched	Recipe	Cl_2 (sccm)	O_2 (sccm)	Ar (sccm)	CF_4 (sccm)	Pressure (mTorr)	Microwave Power (W)	RF Power (W)/ DC Bias (V)
Cr	**Cl_2/O_2 LO**	7.5	1.5	0	0	2	500	110/-150
AlN	**Cl_2/Ar LO**	6	0	1.5	0	2	500	110/-150
Mo	**CF_4/O_2**	0	1.5	0	6	2	500	110/-150

Table 3.9: Approximate material etch rates (Å/min).

Recipe	Cr Etch Rate	AlN Etch Rate	Mo Etch Rate
Cl_2/O_2 LO	~675	~0-100	unknown
Cl_2/Ar LO	~150	~1250-1700	~1500-2000
CF_4/O_2	unknown	unknown	~750

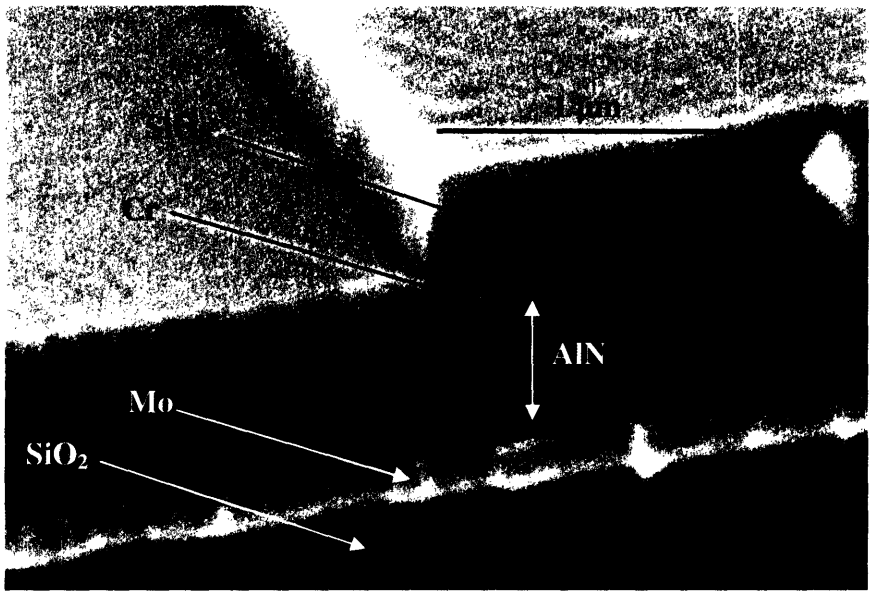

Figure 3.14: Unetched stack of materials with 4000 Å SiO_2 mask.

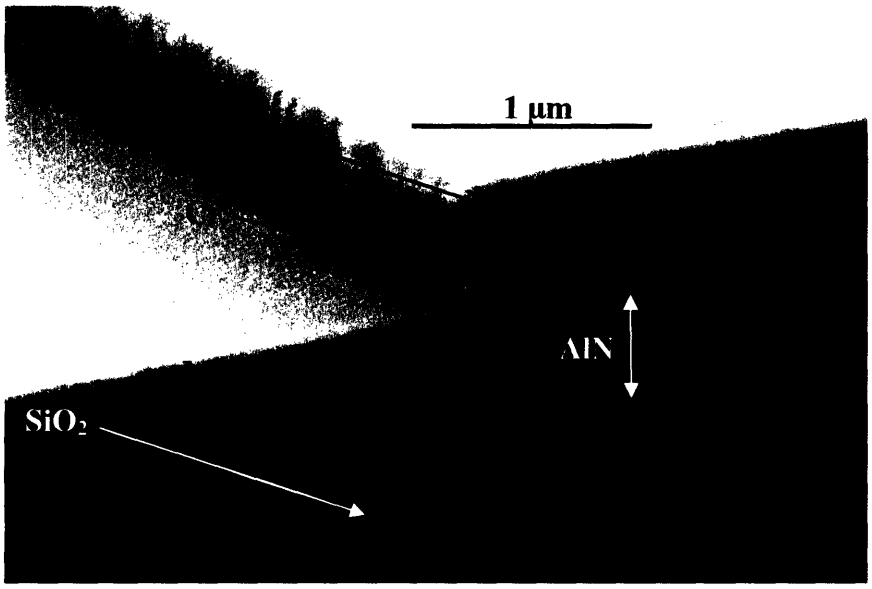

Figure 3.15: Cr etch: After 2 minute 30 second Cl_2/O_2 LO etch.

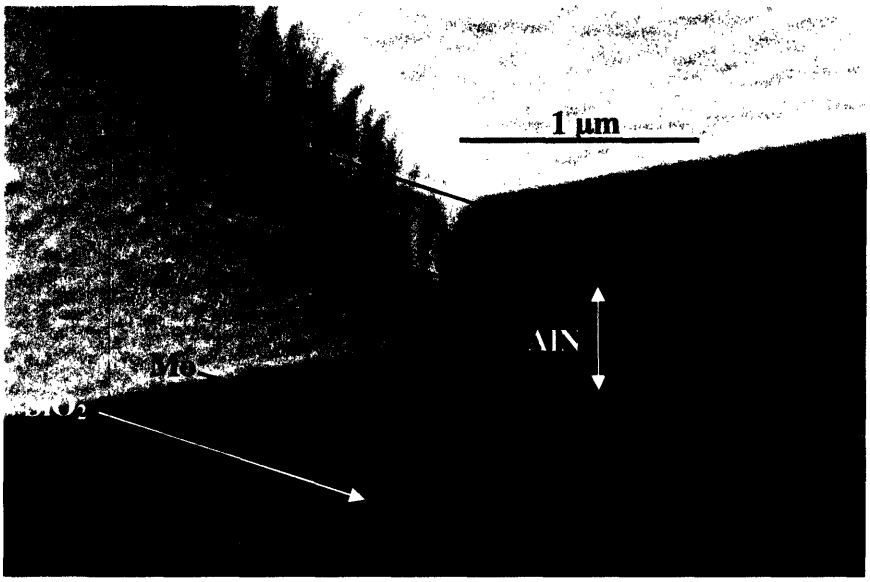

Figure 3.16: Partial AlN etch: After 2 minute 30 second Cl_2/O_2 LO etch and 1 minute Cl_2/Ar LO etch.

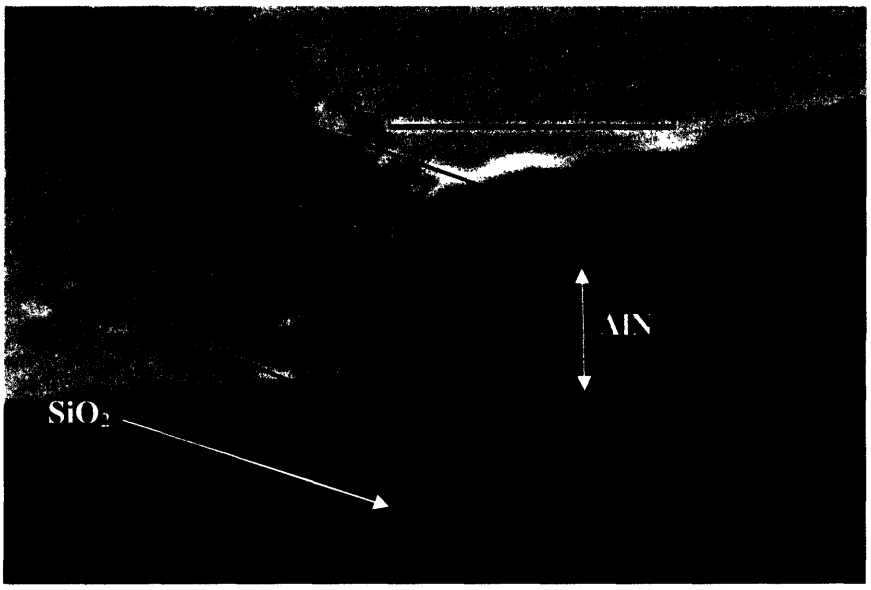

Figure 3.17: Partial AlN etch: After 2 minute 30 second Cl_2/O_2 LO etch and 2 minute 15 second Cl_2/Ar LO etch.

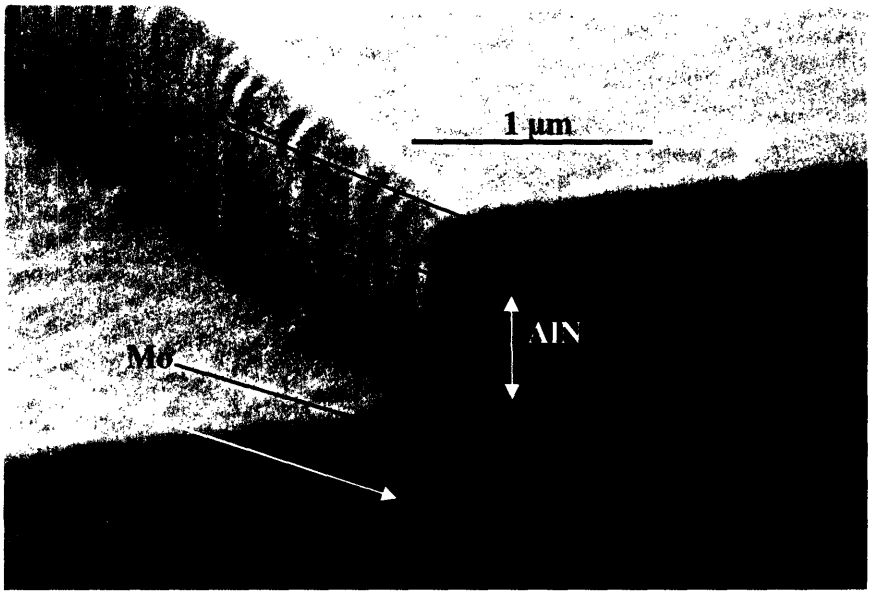

Figure 3.18: AlN etch: After 2 minute 30 second Cl_2/O_2 LO etch and 4 minute Cl_2/Ar LO etch.

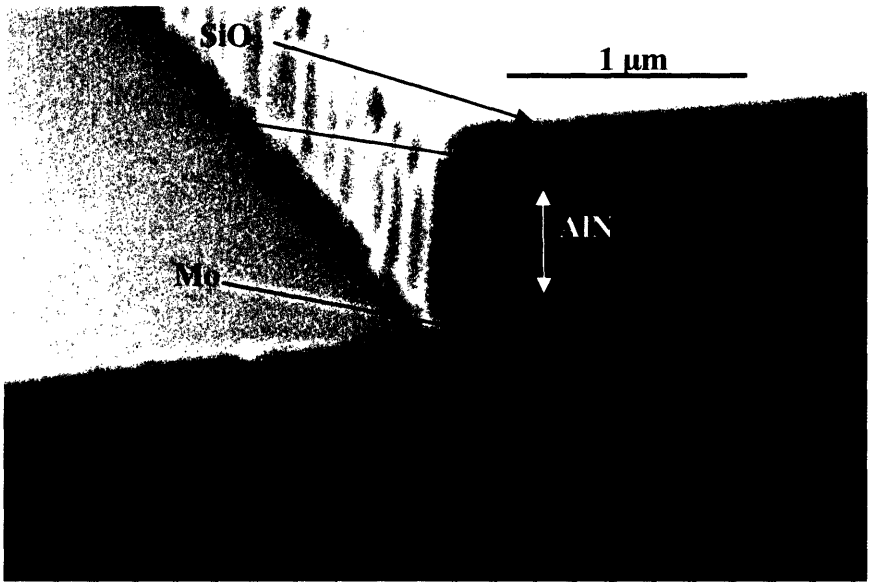

Figure 3.19: Mo etch: After 2 minute 30 second Cl_2/O_2 LO etch, 4 minute Cl_2/Ar LO etch, and 2 min 30 second CF_4/O_2 etch.

3.5 Conclusions

The dry etching experiments showed that an anisotropic etch (>80^{o} measured from horizontal) through the "stack" of materials with no undercut could be achieved by using a combination of Cl_2/O_2, Cl_2/Ar, and CF_4/O_2 plasmas at low pressure (2 mTorr), high microwave/source power (500W), and a moderate DC bias (-150V). However, inconsistent etch rates due to variable chamber conditions require visual monitoring of the samples that are being etched in order to prevent under or overetching of the materials. The etch rate inconsistencies can be somewhat mitigated by running a consistent set of chamber pre-clean etches and a dummy etch sample prior to processing real samples. Even with these precautions and visual endpoint detection, yield, particularly for stopping on the Mo layer, is poor. A switch to a more robust system that doesn't require extensive visual monitoring can be expected to increase yield.

Chapter 4

Device Fabrication Results

The objectives of the new device fabrication process were to eliminate the bond pad ledge produced by the old fabrication process by performing an aligned release and to produce notches and other small features that require a straight sidewall etch. This section presents device fabrication results using the improved process.

4.1 Fabricated Device

Figure 4.1 shows an SEM of a released 3 μm x 25 μm resonator with 750 nm tethers fabricated with the new process and of a 5 μm x 3 μm resonator fabricated with the previous process. The fabrication improvements described in this thesis can be clearly seen in the image of the resonator fabricated with the new device process. The sidewall angle is steeper allowing smaller feature sizes. The tether also clearly makes an abrupt transition from being unsupported to being rigidly connected to the SiO_2 layer. This contrasts with the unsupported ledge seen in the device fabricated with the previous process. The following sections provide further details on these fabrication process improvements.

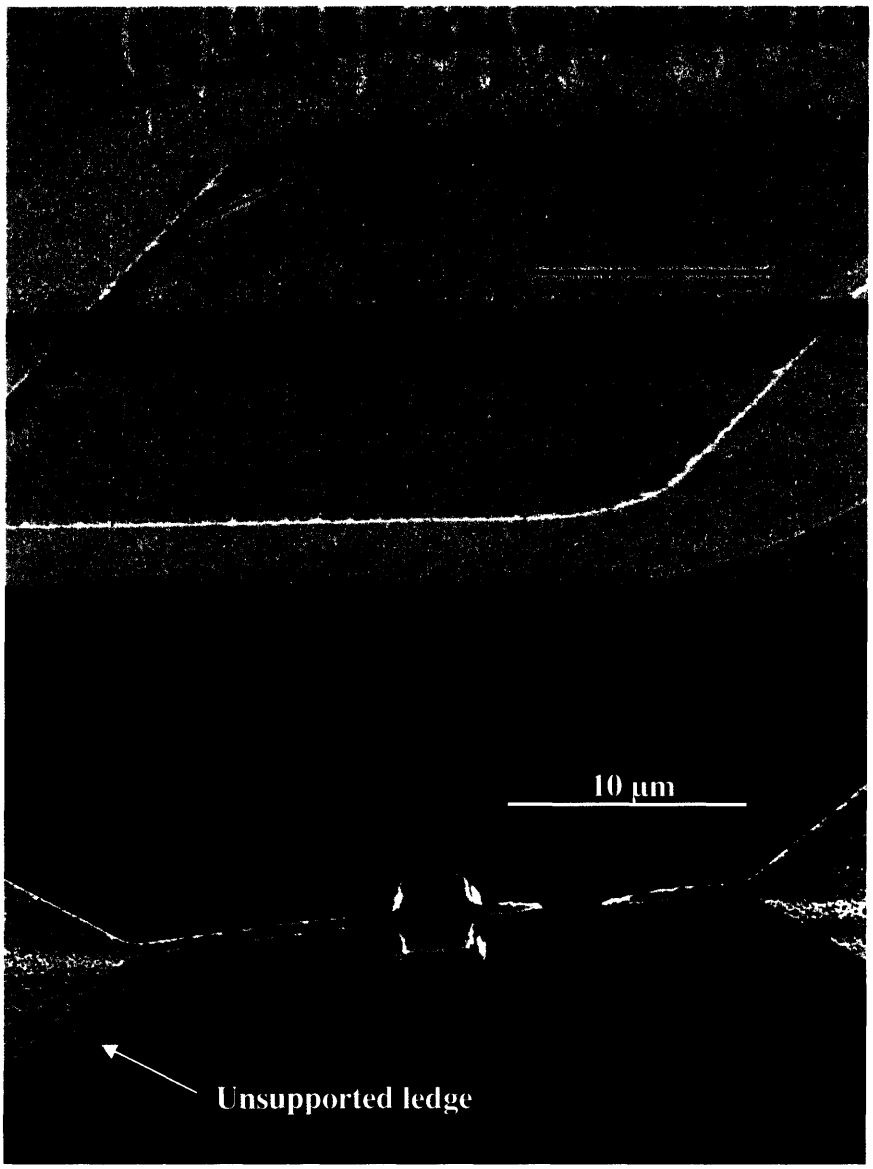

Figure 4.1: Top - Released 3 μm x 25 μm resonator fabricated with modified process; **Bottom –** Released 5 μm x 3 μm resonator fabricated with the previous process. Sidewall angle, feature size, and support structure improvements are evident in the new process.

4.2 Aligned Release

As shown in Figure 4.1, the aligned release of the resonators was effective in eliminating the bond pad ledge that was produced by the old fabrication process. However,

significant drifting of the wafer relative to the mask during the alignment process made an accurate alignment impossible and thus caused the alignment of the release over the wafer to be non-optimal for many resonators. Nevertheless, on one device wafer, for 11 devices located closest to the line between the two alignment marks, an average overlay error of 55 nm (110 nm min-max) was measured. The overlay error was determined by taking half the difference of the distance between the left side of the resonator and the resist window and the right side of the resonator and the resist window. A measurement uncertainty was assumed to be ± 1 pixel, which corresponds to ~ ± 50 nm. Figure 4.2 shows a resonator with a perfectly aligned (~ ± 50 nm in x-direction) release etch window. Measurements were determined by optimal micrographs. It is important to note that for the release of a resonator, the misalignment of the release window in the x-direction is of most importance since that is what will determine the tether length for each side of the resonator. Away from the line between the two marks, the X error increased significantly due to θ misalignment.

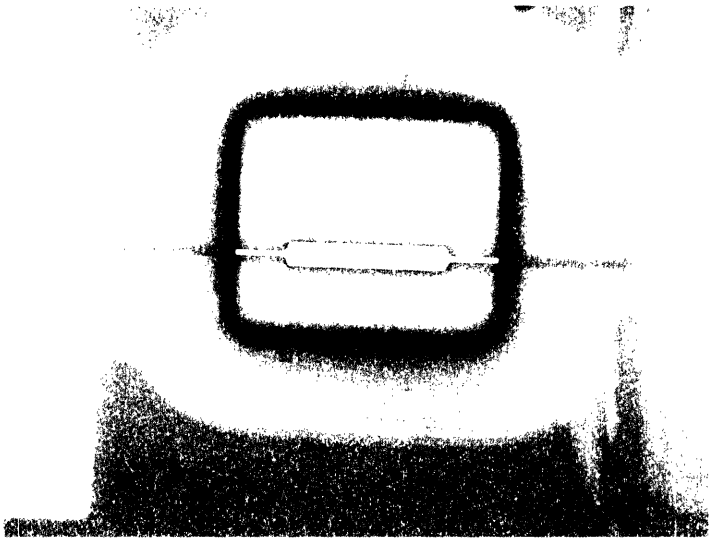

Figure 4.2: Perfectly aligned (~ ± 50 nm in x-direction) release etch window.

The alignment drift is believed to be caused by the wafer slipping after the mask and wafer are released from intimate contact or while they're going into contact. It is suspected that vacuum grease which was applied to the back of the wafers for the stack Cl-based ECR etches prevents good mechanical contact between the vacuum chuck and

the wafer. However, there could very well be other contributors to the drift. After removing the residual grease from the back of the wafer and the wafer chuck, the drift was still present, albeit to a lesser degree. It is possible that either the θ-stage or one of the clamps that hold the θ piezo-actuator and manual micrometer was slipping.

In future fabrications, the alignment drift due to the vacuum grease can be eliminated by either performing a thorough clean of the vacuum grease immediately after performing the stack etch or by simply not using it anymore. The latter option would require some other method of keeping the wafer securely fastened to the ECR load arm since it has the tendency to slide when no vacuum grease is applied to its backside. It is also worth investigating whether or not there are other sources of drift. A simple way to determine this would be to perform an alignment with a different mask and a wafer with a clean backside.

4.3 Notches and Small Features

The new fabrication process also demonstrated the ability to produce notches and other small features due to the straight sidewalls produced by the Cl-based dry etch of the stack. Figure 4.3 and 4.4 show 0.5 μm notches at the resonator-tether interface produced by the new fabrication process. Figure 4.5 shows a 1 μm x 50 μm resonator with 0.5 μm tethers.

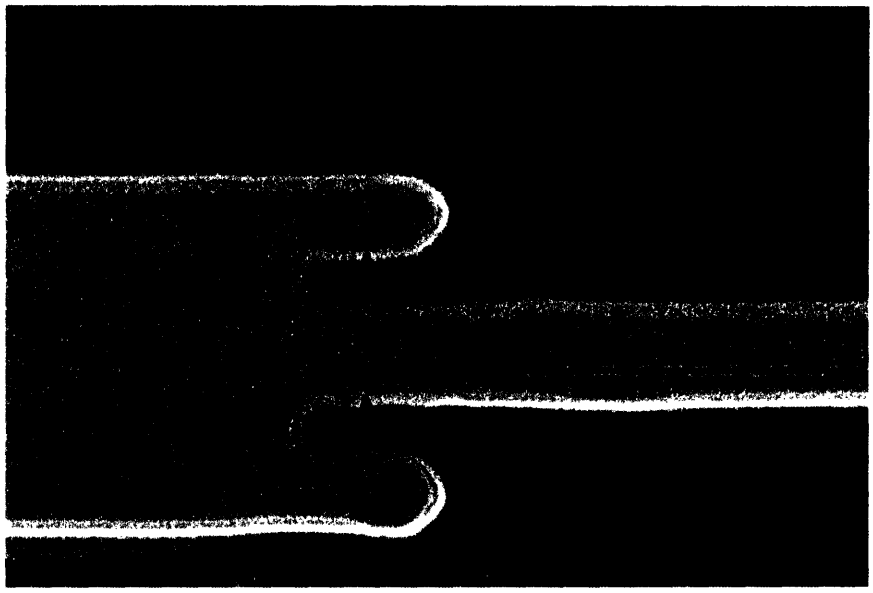

Figure 4.3: Top view of 0.5 μm notches at the resonator-tether interface.

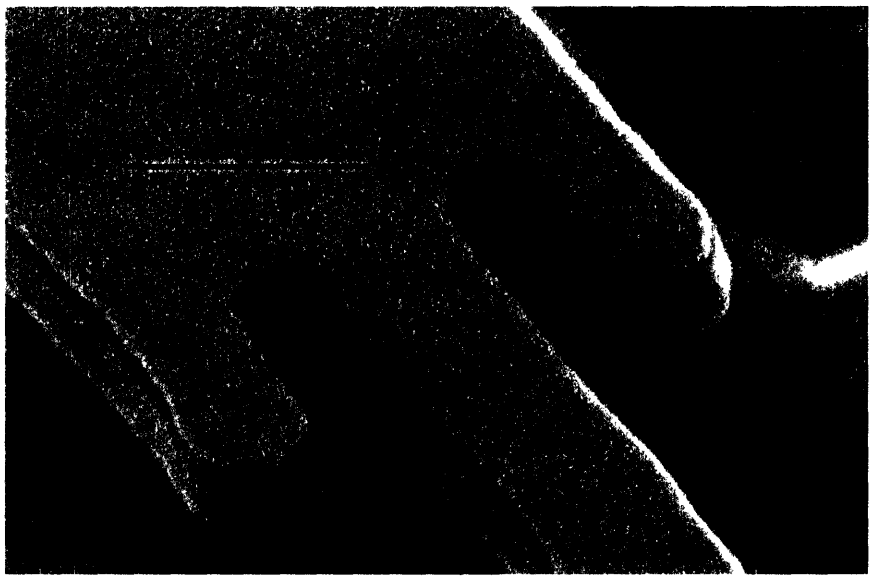

Figure 4.4: Angle view of 0.5 μm notches at the resonator-tether interface.

Figure 4.5: 1 μm x 50 μm resonator with 0.5 μm tethers.

Chapter 5

Summary and Conclusions

5.1 Summary

Fabrication process changes were proposed to modify the mechanical structure of the Draper L-bar resonator to potentially increase Q and improve the frequency range. The process changes were: conformable contact lithography (CCL), moiré alignment, and chlorine dry etching. The new fabrication process aimed to increase Q by eliminating an undesirable bond pad ledge with an aligned release (CCL/moiré alignment) and by allowing the inclusion of notches at the resonator-tether interface (CCL/Cl-based dry etch). It also aimed to increase the frequency range of the resonator by reducing feature sizes (CCL/Cl-based dry etch).

The background and theory behind conformable contact lithography and moiré alignment were discussed. An automated alignment system was described and demonstrated a simulated alignment accuracy of less than 100 nm for a single set of alignment marks. A non-automated alignment experiment was conducted to determine the pattern placement accuracy of the current CCL/moiré alignment system. Mean pattern placement errors of $|0.187\ \mu m|$ and $|0.296 \mu m|$ were recorded for the x- and y-directions respectively.

A literature review for the etching of Cr, AlN, and Mo was presented. The wet etch that produced a sloped sidewall angle in the old fabrication process was also discussed and demonstrated the need for a Cl-based dry etch of the "stack" materials. Cl-based dry etch experiments conducted at the Harvard University Center for Nanoscale Systems (CNS) were discussed. The experiments demonstrated that a straight sidewall angle ($>80^{o}$ measured from horizontal) through the "stack" of materials with no undercut could be achieved by using a combination of Cl_2/O_2, Cl_2/Ar, and CF_4/O_2 plasmas at low pressure (2 mTorr), high microwave/source power (500W), and a moderate DC bias (-150V).

Device fabrications showed that the process changes eliminated the undesirable bond pad ledge and improved the sidewall angle of the resonator. For the aligned release, an average overlay error of 55 nm (110 nm min-max) was measured for 11 devices located closest to the line between the two alignment marks in spite of significant alignment drift. The steep sidewall angle allowed the patterning of notched resonator-tether interfaces and other small feature sizes (~0.5 μm). Even smaller feature sizes are possible with the improved sidewall angle.

5.2 Future Work

Modifications and refinements to the current CCL/moiré alignment will likely yield improved alignment accuracies. Sub-100 nm alignment accuracies seem to be a reasonable expectation in the future and are necessary if an aligned release of high frequency resonators is desired. An automated alignment system may also be a future possibility if the current CCL/moiré alignment setup is improved upon.

A more consistent etch system for the "stack" etch is necessary for respectable device yields. In addition, an etch recipe that will either etch through all three layers of the "stack" or "stop" on the Mo would be an ideal process and may be worth further investigation.

With the addition and refinement of the process changes, future device fabrication holds the potential for achieving higher Q factors and frequencies than previously demonstrated.

Appendix A

Aligned Printing Procedure

This appendix presents the step-by-step procedure for performing an aligned print with the LiLCo Systems CCA-M4 Conformable Contact Aligner to include the modifications (Z-stage, piezo-actuators, etc.) discussed in Chapter 3.

- Turn on exposure lamp and allow it to adequately warm up (~1 hour).
- Turn on computer, start camera/microscope imaging software, and Z-stage control software.
- Set all rocker switches on the remote console to their middle position.
- Turn on POWER and PUMP rocker switches located on the main chassis.
- Move the dual microscopes to their rear position (if not there already) by pressing the "scopes" rocker switch on the remote console to the EXPOSE position. Put the switch back to its middle position when this is completed.
- Move the aligner head to the center of the table (if not there already) underneath the dual-microscope rails by pressing the "aligner" rocker switch on the remote console to the ALIGN position. Put the switch back to its middle position when this is completed.
- Set the mask in the mask holding plate with the pattern absorbers down.
- Bring the dual-microscopes to the forward position by pressing the "scopes" rocker switch on the remote console to the ALIGN position. Put the switch back to its middle position when this is completed.
- Turn the microscopes on by pressing the center rocker switch on the remote console to its ON position. The green LED located above the switch should light.
- Center the alignment marks under each microscope by rotating the mask. (Be sure to push the mask towards the rear while doing this such that the mask is contacting the two rear mask retaining clips.) This will require moving the dual-microscope head in X and Y directions with the manual micrometers located behind the dual-microscopes. It may also require moving each individual

microscope by loosening the hex-screw found on the rear of each microscope. The microscope focus, tilt, illumination, and resolution settings may also need adjustments.

- Move the dual-microscopes to the rear position.
- Blow the wafer chuck, wafer back, and wafer front clean with dry, filtered air.
- Place the wafer on the wafer chuck.
- Move the dual-microscopes to the forward position and put the switch back to its middle position.
- Move the wafer on the wafer chuck so that the alignment marks are roughly aligned under the microscopes. In order to focus on the wafer, it may be easier to move the Z-stage up (+ direction) instead of adjusting the focus knob.
- Press the lower-right rocker switch on the remote console to the CHUCK position. Confirm that the wafer is being held securely in place by gently pushing on the side of the wafer.
- Use the X, Y, and θ substrate adjustments (manual micrometers or piezos) to center the alignment marks on the wafer under the microscopes.
- Perform rotation to calculate center of rotation (future)
- Move the dual-microscopes back to the rear position.
- Move the Z-stage back to its original position if it was elevated. Failure to do so may result in damage to the mask and wafer when the mask is put in its holding plate!
- Blow the wafer and mask clean with dry, filtered air.
- Place the mask in the mask holding plate.
- Bring the dual-microscopes to their forward position.
- Rotate the mask until the alignment marks are centered under the microscopes. (Be sure to push the mask towards the rear while doing this such that the mask is contacting the two rear mask retaining clips.)
- Secure the mask in place by pushing the front mask-retaining clip down and back against the mask ring while tightening the clamp screw.

- Press the "contact/release" rocker switch on the remote console to it CONTACT position.
- Adjust the fine contact gauge with the contact-vacuum control located on the remote console until the gauge reads ~2"-3" WC.
- Move the Z-stage up by 200 μm increments until the gauge deflects to the right.
- Adjust the gauge to ~6" WC.
- Press the "contact/release" rocker switch to its RELEASE position.
- Observe the fine release-pressure gauge located on the main control chassis and set the pressure to ~1 mm WC with the release pressure knob to the left of the gauge.
- Bring the Z-stage up by 100 μm and bring the mask into CONTACT. Look for an area of small contact (about the size of a dime).
- If there is no contact point, press the RELEASE the mask and repeat the previous step, otherwise proceed to the next step.
- Note the position of the small contact area and RELEASE the mask.
- Make adjustments to the three mask-height micrometers to center the small contact area. Increasing the values on the micrometers lowers the mask plate.
- Bring the mask back into CONTACT. If the small contact area is still not centered, RELEASE the mask and go back to the previous step. (Leveling the mask may cause a loss of contact with the wafer and require subsequent Z-stage adjustments).
- RELEASE the mask and raise the Z-stage by 50 μm
- Roughly align the alignment marks by adjusting the focus knob in order to obtain blurred images of the two marks on the wafer and the two on the mask.
- Bring the mask into CONTACT.
- Slowly increase the contact vacuum until at least 80% of the mask is in intimate contact. Note the necessary alignment corrections (X, Y, θ, Magnification). (The microscope focus, tilt, illumination, and resolution settings may need adjustments in order to obtain the best possible images).

- RELEASE the mask, make the necessary alignment corrections, and bring the mask back into CONTACT. (It is important to never move the wafer while there is intimate contact between the mask and wafer. Doing so can cause the mask to be damaged or scrape up clumps of resist which will prevent intimate contact).
- Repeat the previous step until alignment is achieved.
- Press the "aligner" switch to its EXPOSE position. This will move the aligner head to the exposure lamp.
- Expose the substrate
- Press the "aligner" switch to its ALIGN position. Move the switch back to its middle position once the aligner head is back underneath the dual-microscopes.
- Slowly reduce the contact vacuum to less than 6" WC.
- RELEASE the mask.
- Lower the Z-stage back to its starting position.
- Loosen the front mask-retaining clip and remove the mask.
- Press wafer-chucking switch to its middle position and remove the wafer.
- Turn off all equipment

Appendix B

Overview of Automated Alignment Algorithm

This appendix describes the automated alignment algorithm used for the alignment simulation (one set of alignment marks). For a real alignment, the algorithm would differ slightly since live images would be imported in addition to taking θ and magnification error into account since there would be two sets of alignment marks. All programming and analysis was performed with National Instruments Labview 7.1 and Vision 7.1.

- Based on user input, create matching pair of marks.
- Misalign the simulated wafer mark a random distance and direction.
- Move the marks to a random location in the image window.
- Resample image of combined marks to a size of 400 pixels x 400 pixels. This is close to the resolution of a real image (640 pixels x 480 pixels).
- Blur image with IMAQ Convolute to simulate a real image.
- Add 5% Gaussian White Noise to simulate a real image.
- Find centroid of the marks with IMAQ Count Objects.
- Display image and ask user whether to do a "Coarse" or "Fine" alignment.

Coarse Alignment

- Have user draw a line parallel to the rear of the "spider" using IMAQ Construct ROI.
- Have user input the number of fringes in contact with the center of the marks. This value multiplied by ½ the pitch width is the magnitude of the "coarse shift."
- Based on the user drawn line, determine the direction of the "coarse shift."
- Shift the simulated wafer mark in the direction and magnitude specified by the user inputs.
- Display marks after they are coarsely aligned.
- Proceed to Fine Alignment.

Fine Alignment

- Using IMAQ Light Meter, perform 360 radial light scans from the centroid of the marks at 1^{o} increments.
- Plot pixel intensity versus distance from centroid for all 360 light scans. Convert the light scan distances (which are determined by nearest pixel) and convert that to an actual pixel distance.
- Using Threshold Peak Detector, determine the moiré fringe location.
- Determine a best fit for the detected location points using Levenberg Marquardt.
- Plot distance (center to fringe) versus angle for the best fit and actual data.
- Based on the moiré fringe misalignment determined by the best fit, shift the wafer mark so that the marks are realigned. The distance that the wafer mark is shifted is a fraction of the moiré fringe misalignment. This fraction is determined by the "shift factor" as described in Chapter 2.
- Display the aligned marks.
- Determine the alignment error by comparing the randomly generated misalignment distance and direction to the alignment corrections that were made (coarse + fine).

Appendix C

PECVD SiO_2 Reactive Ion Etch with Fluorine-based Plasma

This appendix presents additional information about the PECVD SiO_2 RIE etch with F-based plasma. Table A3.1 presents the etch recipe used. Figure A3.1 shows etch depth vs. time. Etch depth was determined by ellipsometer measurements of blanket films. A linear fit of the data gives an etch rate of ~860 Å/min. Figure A3.2 shows a 2.5 minute (~10% overetch) etch of the SiO_2 with Shipley 1813 resist acting as an etch mask. The SiO_2 etched cleanly with straight sidewalls.

Table C.1: Etch recipe for RIE patterning of PECVD SiO_2 mask

CHF_3 (sccm)	CF_4 (sccm)	Pressure (mTorr)	RF Power (W)/ DC Bias (V)
14.4	1.6	5.0	130/475

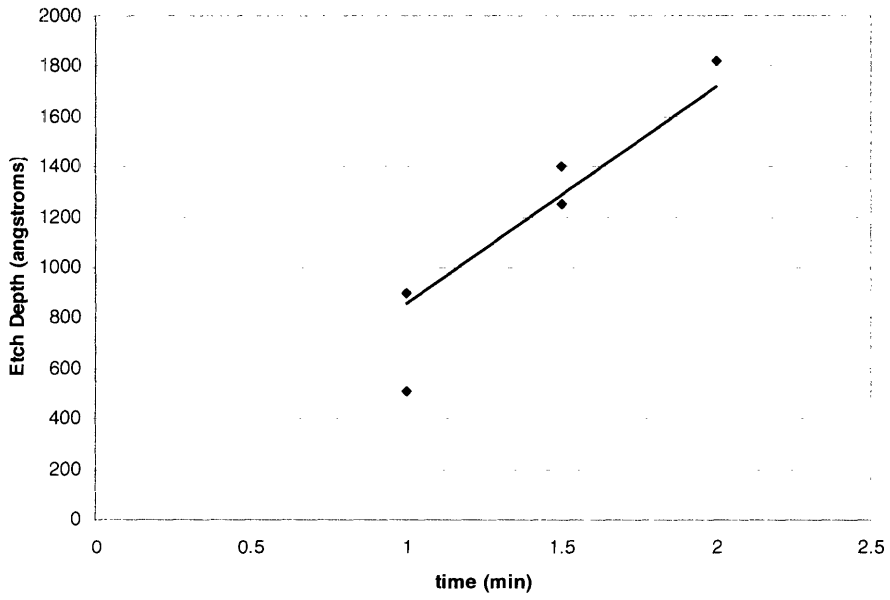

Figure C.1: Etch depth vs. time of PECVD SiO_2 in F-based plasma

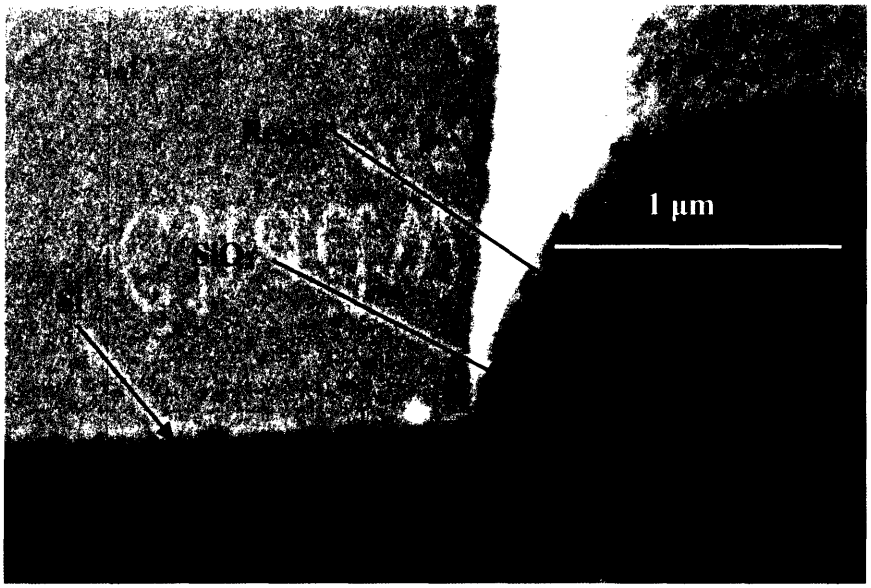

Figure C.2: 2.5 minute (~10% overetch) etch of the SiO_2 with F-based plasma

Appendix D

ECR Etch Procedure

The general procedure for performing an ECR etch at the Harvard University CNS is described below.

- Flip "gas request" switch on the scrubber control to the ON position. Wait for the green LED to light and make sure no alarms are triggered.
- Log into computer system with username and password.
- Make sure substrate (quartz mounted on Si wafer) is on load arm.
- Clean and prep the chamber by running "Chamber Burn In" recipe followed by "O_2 Clean" recipe.
- Condition the chamber by running the upcoming etch recipe for 5 min. (It is a good idea to condition the chamber whenever the recipe is changed).
- Vent the load lock and load the sample onto the quartz substrate. Apply a dab of vacuum grease to the back of the sample to prevent it from sliding off of the substrate.
- Run the recipe.
- Unload the sample.
- Remove excess vacuum grease from quartz substrate with a cleanroom wipe. Swab with acetone if necessary.
- Pump the load lock down.
- Log off system.
- Flip "gas request" switch to the OFF position.
- Record performed etches in log book.

A more detailed procedure specifically for performing the ECR stack etch at the Harvard University CNS is described below.

- Flip "gas request" switch on the scrubber control to the ON position. Wait for the green LED to light and make sure no alarms are triggered.
- Log into computer system with username and password.
- Make sure substrate (quartz mounted on Si wafer) is on load arm.
- Clean and prep the chamber by running "Chamber Burn In" recipe followed by "O_2 Clean" recipe.
- Condition the chamber for the Cr etch by running "DraperCr" for 5 min.
- Vent the load lock and load a stack test piece onto the quartz substrate. Apply a dab of vacuum grease to the back of the piece to prevent it from sliding off of the substrate.
- Run "DraperCr" for 2 minutes 30 seconds.
- Check to make sure that the Cr is completely etched. The underlying AlN will appear pink or green depending on the angle at which you look at the sample.
- If the Cr is cleared unload the sample, otherwise run the recipe at 30 second increments until this is achieved. (Overetching the Cr is far better than leaving a little bit of Cr).
- Condition the chamber for the AlN etch by running "DraperAl" for 5 min.
- Vent the load lock and load the test piece onto the quartz substrate. Apply a dab of vacuum grease to the back of the piece to prevent it from sliding off of the substrate.
- Run "DraperAl" for 3 minutes.
- Check to see if the AlN is completely etched. The underlying Mo will appear metallic or silver in color.
- If the AlN is cleared, unload the test piece and note the etch time. Otherwise run the recipe at 30 second increments until this is achieved. Be sure to note the amount of time it took to etch through the AlN.
- Condition the chamber for the Mo etch by running "DraperMo" for 5 min.
- Vent the load lock and load the test piece onto the quartz substrate. Apply a dab of vacuum grease to the back of the piece to prevent it from sliding off of the

substrate if needed. There may be enough grease remaining on the back of the test piece.

- Run "DraperMo" for 2 minutes.
- Check to see if the Mo is completely etched. The underlying SiO_2/AlN "seed" layer will appear pink or green depending on the angle at which you look at the sample.
- If the Mo is cleared, unload the test piece and note the etch time. Otherwise run the recipe at 30 second increments until this is achieved. Be sure to note the amount of time it took to etch through the Mo.
- Condition the chamber for the Cr etch of the real samples by running "DraperCr" for 5 min.
- Vent the load lock and load the sample onto the quartz substrate. Apply a dab of vacuum grease to the back of the sample to prevent it from sliding off of the substrate.
- Run "DraperCr" for the amount of time it took to clear the Cr for the test piece.
- Check to make sure that the Cr is completely etched.
- If the Cr is cleared unload the sample, otherwise run the recipe at 30 second increments until this is achieved.
- Repeat the previous 4 steps for each sample.
- Condition the chamber for the AlN etch by running "DraperAl" for 5 min.
- Vent the load lock and load the sample onto the quartz substrate. Apply a dab of vacuum grease to the back of the sample if necessary.
- Run "DraperAl" for no longer than 75% of the time that it took to clear the AlN for the test piece.
- Check to see if the AlN is cleared.
- If the AlN is cleared, unload the sample. Otherwise, continue at increments no greater than 30 seconds until the AlN is cleared.
- Repeat the previous 4 steps for each sample.
- Condition the chamber for the Mo etch by running "DraperMo" for 5 min.

- Vent the load lock and load the sample onto the quartz substrate. Apply a dab of vacuum grease to the back of the sample if necessary.
- Run "DraperMo" for the amount of time it took to clear the Mo for the test piece.
- Check to make sure that the Mo is completely etched.
- If the Mo is cleared, unload the sample, otherwise run the recipe at 30 second increments until this is achieved.
- Repeat the previous 4 steps for each sample.
- Remove excess vacuum grease from quartz substrate with a cleanroom wipe. Swab with acetone if necessary.
- Pump the load lock down.
- Log off system.
- Flip "gas request" switch to the OFF position.
- Record performed etches in log book.

References

[1] Sharma, R.K., Ning, J., Hanhua, F., and Gopalakrishnan, R., "Process Development and Integration of Piezoelectric Aluminum Nitride Thin-Film for RF MEMS Applications," *Materials Research Society Symposium Proceedings*, Vol. 741, 2003, pp. 169-174.

[2] Lakin, K.M., "Thin Film Resonators and Filters," *1999 IEEE Ultrasonics Symposium*, Bend, Oregon, 1999, pp. 895-906.

[3] Antkowiak, B., Gorman, J.P., Varghese, M., Carter, D.J.D., Duwel, A.E., "Design of a High-Q, Low-Impedance, GHz-Range Piezoelectric MEMS Resonator," *The 12th International Conference on Solid-State Sensors, Actuators, and Microsystems (Transducers)*, Boston, MA, June 2003, pp. 841-846.

[4] Carter, D.J.D., Kang, J., White, D., Duwel, A.E., "Fabrication and Measurement of an IC-Compatible GHz-Range Piezoelectric Longitudinal Bar Resonator," *Solid-State Sensor, Actuator, and Microsystems Workshop*, Hilton Head, South Carolina, June 6-10 2004.

[5] Carter, D.J.D., Charles Stark Draper Laboratory, Inc., personal communication

[6] Calhoun, P.J., "Frequency Synthesis using MEMS Piezoelectric Resonators," The Charles Stark Draper Laboratory, Inc., CSDL-T-1485, Cambridge, MA, June 2004.

[7] Hohreiter, L.A., "The Effects of Mechanical Coupling on the Electrical Impedance of MEMS Resonators for UHF Filter Applications," The Charles Stark Draper Laboratory, Inc., CSDL-T-1490, Cambridge, MA, June 2004.

[8] Li, S.S., Lin, Y.W., Xie, Y., Ren, Z., Nguyen, C.T.C., "Micromechanical "Hollow-Disk" Ring Resonators," *IEEE MEMS '04*, pp. 821-824.

[9] Piazza, G., Stephanou, P.J., Porter, J.M., Wijesundara, M.B.J., Pisano, A.P., "Low Motional Resistance Ring-Shaped Contour-Mode Aluminum Nitride Piezoelectric Micromechanical Resonators for UHF Applications," *18th IEEE International Conference on Micro Electro Mechanical Systems (MEMS2005)*, Miami, Florida, January 30-February 3, 2005.

[10] Goodberlet, J.G., "Multi-Level Alignment Accuracy Below 35 nm with Conformable-Contact Photolithography," private correspondence.

[11] Madou, M.J., Fundamentals of Microfabrication: The Science of Miniaturization, 2nd ed., CRC Press, Boca Raton, FL, 2002, pp. 20-21.

[12] Goodberlet, J.G., "Patterning 100 nm Features Using Deep –Ultraviolet Contact Photolithography," *Applied Physics Letters,* Vol. 76, No. 6, February 2000, pp. 667-669.

[13] Biebuyck, H.A., Larsen, N.B., Delamarche, E. and Michel, B., "Lithography Beyond Light: Microcontact Printing with Monolayer Resists," *IBM Journal of Research and Development*, Vol. 41, No. ½, January/March 1997, pp. 159-170.

[14] Rogers, J.A., Paul, K.E., and Whitesides, G.M., "Quantifying Distortions of Soft Lithography," *Journal of Vacuum Science and Technology B*, Vol. 16, No. 1, January/February 1998, pp. 88-97.

[15] King, M.C. and Berry, D.H., "Photolithographic Mask Alignment Using Moiré Techniques," *Applied Optics*, Vol. 11, No. 11, November 1972, pp. 2455-2459.

[16] Park, Y.C. and Kim, S.W., "Determination of Two-Dimensional Planar Displacement by Moiré Fringes of Concentric-Circle Gratings," *Applied Optics*, Vol. 33, No. 22, August 1994, pp. 5171-5176.

[17] Milenin, A.P., Jamois, C., Wehrspohn, R.B., Reiche, M., "The SOI Planar Photonic Crystal Fabrication: Patterning of Cr Using Cl_2/O_2 Plasma Etching," *Microelectronic Engineering*, Vol. 77, 2005, pp. 139-143.

[18] Nakata, H., Nishioka, K., Abe, H., "Plasma Etching Characteristics of Chromium Film and its Novel Etching Mode," *Journal of Vacuum Science and Technology,* Vol. 17, No. 6, November/December 1980, pp. 1351-1357.

[19] Mileham, J.R., Pearton, S.J., Abernathy, C.R., Mackenzie, J.D., Shul, R.J., and Kilcoyne, S.P., "Wet Chemical Etching of AlN," *Applied Physics Letters*, Vol. 67, No. 8, August 1995, pp. 1119-1121.

[20] Mileham, J.R., Pearton, S.J., Abernathy, C.R., Mackenzie, J.D., Shul, R.J., and Kilcoyne, S.P., "Patterning of AlN, InN, and GaN in KOH-Based Solutions," *Journal of Vacuum Science and Technology A*, Vol. 14, No. 3, May/June 1996, pp. 836-839.

[21] Vasnyov, S., "Investigation of the Correlation of Electronic and Dynamic Dislocation Properties in ZnO," Martin-Luther-Universität Halle-Wittenberg, Kyiv, Ukraine, April 1974.

[22] Zhuang, D., Edgar, J.H., Liu, L., Liu, B., and Walker, L., "Wet Chemical Etching of AlN Single Crystals," *MRS Internet Journal of Nitride Semiconductor Research*, Vol. 7, No. 4, 2002.

[23] Kitamura, S., Hiramatsu, K., and Sawaki, N., "Fabrication of GaN Hexagonal Pyramids on Dot-Patterned GaN/Sapphire Substrates via Selective Metalorganic Vapor Phase Epitaxy," *Japanese Journal of Applied Physics*, Vol. 34, No. 9B, September 1995, pp. 1184-1186.

[24] Eddy, C.R., "Etch Processing of III-V Nitrides," *MRS Internet J. Nitride Semicond.*, Res. 4S1, G10.5, 1999.

[25] Shul, R.J., Zhang, L., Willison, C.G., Han, J. Pearton, S.J., Hong, J., Abernathy, C.R., Lester, L.F., "Group-III Nitride Etch Selectivity in BCl_3/Cl_2 ICP Plasmas," *MRS Internet J. Nitride Semicond.*, Res. 4S1, G8.1, 1999.

[26] Shul, R.J., Willison, C.G., Bridges, M.M., Han, J., Lee, J.W., Pearton, S.J., Abernathy, C.R., MacKenzie, J.D., Donovan, S.M., Zhang, L., Lester, L.F., "Selective Inductively Coupled Plasma Etching of Group-III Nitrides in Cl_2- and BCl_3-based Plasmas," *Journal of Vacuum Science and Technology A*, Vol. 16, No. 3, May/June 1998, pp. 1621-1626.

[27] Pearton, S.J., Abernathy, C.R., Ren, F., Lothian, J.R., Wisk, P.W., Katz, A., "Dry and Wet Etching Characteristics of InN, AlN, and GaN Deposited by Electron Cyclotron Resonance Metalorganic Molecular Beam Epitaxy," *Journal of Vacuum Science and Technology A*, Vol. 11, No. 4, July/August 1993, pp.1772-1775.

[28] Vartuli, C.B., Mackenzie, J.D., Lee, J.W., Abernathy, C.R., Pearton, S.J., Shul, R.J., "Cl_2/Ar and CH_4/H_2/Ar Dry Etching of III-V Nitrides," *Journal of Applied Physics*, Vol. 80, No. 7, 1 October 1996, pp. 3705-3709

[29] Shul, R.J., Kilcoyne, S.P., Crawford, M.H., Parmeter, J.E., Vartuli, C.B., Abernathy, C.R., Pearton, S.J., "High Temperature Electron Cyclotron Resonance Etching of GaN, InN, and AlN," *Applied Physics Letters*, Vol. 66, No. 14, 3 April 1995, pp. 1761-1763.

[30] Pearton, S.J., Abernathy, C.R., Ren, F., "Low Bias Electron Cyclotron Resonance Plasma Etching of GaN, AlN, and InN," *Applied Physics Letters*, Vol. 64, No. 17, 25 April 1994, pp. 2294-2296.

[31] Ha, D., Takeuchi, H., Choi, Y.K., King, T.J., "Molybdenum Gate Technology for Ultrathin-Body MOSFETs and FinFETs," *IEEE Transactions of Electron Devices,* Vol. 51, No. 12, December 2004, pp. 1989-1996.

[32] Picard, A. and Turban, G., "Plasma Etching of Refractory Metals (W, Mo, Ta) and Silicon in SF_6 and SF_6-O_2. An Analysis of the Reaction Products," *Plasma Chemistry and Plasma Processing*, Vol. 5, No. 4, 1985, pp. 333-351.

[33] Kuo, Y, Crowe, J.R., "Slope Control of Molybdenum Lines Etched with Reactive Ion Etching," *Journal of Vacuum Science and Technology*, Vol. 8, No. 3, May/June 1990, pp. 1529-1532.